DIFFERENTIAL POLARIZATION IMAGING

II. Symmetry Properties and Calculations

MYEONGHEE KIM, LAURA ULIBARRI, AND CARLOS BUSTAMANTE
Department of Chemistry, The University of New Mexico, Albuquerque, New Mexico 87131

ABSTRACT Various differential polarization images or Mueller images of model objects are generated using the equations derived in the previous paper (paper I of this series). These calculated images include models of the higher-order organization of metaphase chromosomes, and show the applicability of the differential polarization imaging method to the elucidation of complex molecular organizations. Then, the symmetry behavior of the Mueller matrix elements upon infinitesimal rotations of the optical components about the optical axis of the imaging system is presented. It is shown that the rotational properties of the Mueller images can be used to eliminate the linear polarization contributions to the M_{14} and M_{44} images, which appear when these images are generated with imperfect circular polarizations. The relationships between the 16 bright-field Mueller images for four different media, i.e., linearly and circularly isotropic, circularly anisotropic, linearly anisotropic, and linearly and circularly anisotropic, are also derived. For the first three cases simple relationships between the Mueller images are found and phenomenological equations in terms of the optical coefficients are derived. In the last case there are no specific relationships between the Mueller images and instead we briefly present Schellman and Jensen's method for treating this type of medium. The criterion of spatial resolution between adjacent domains of different optical anisotropy is then derived. It is found that in transitions between domains of opposite anisotropy the classical Rayleigh limit must be replaced by a magnitude criterion which depends on the limits of the sensitivity of the detection. Finally, the feasibility of optical sectioning in differential polarization imaging is demonstrated.

I. INTRODUCTION

In the first paper of this series (hereafter referred to as paper I), we have presented the derivation of a theory describing how to obtain the differential polarization images of an object that interacts preferentially with one polarization of light over another. To this end, it was first necessary to choose a suitable formalism to describe the state of polarization of the light and its modification upon interaction with the object. We chose the Mueller formalism because it provides the most complete description of the interaction of an object with light of an arbitrary polarization. It was shown that 16 polarization-dependent images, containing useful and complementary structural information about the object, can be obtained. Furthermore, since the ability to discriminate between different states of polarization of light is related to the optical anisotropy of the object imaged, it was shown that these images represent maps of the optical anisotropy of the object. The 16 images, that we have called the Mueller images of the object, are obtained by subtracting the intensities of the light scattered or transmitted by the object when it is illuminated by orthogonal polarization states of light. The theory was derived for an object of arbitrary shape and structure, using the paraxial and thin lens approximations. The equations obtained for each of the 16 Mueller images depend on the incident polarization of the light, the polarization component being analyzed, the internal structure of the object, and the imaging geometry.

The first prototypes of differential polarization microscopes have recently been built (1, 2), and the first differential polarization images have been reported (1–3). Thus, it is of interest to use the theory derived in paper I to investigate the various symmetry properties of the Mueller images, the relationships between them, the relations describing the spatial resolution, and depth of field in these images. These studies will provide a better understanding of the structural information and specificity provided by each of the Mueller images and will guide the experimentalist in generating the Mueller images most appropriate for studying the structure of a given specimen.

This paper is organized as follows: Section II will discuss the programming strategies used in the computations, and the nature and range of validity of the approximations used in the theory. Also the Mueller images of two model objects will be presented and discussed. In section III, the symmetry properties of the Mueller matrix entries and their behavior under rotations about the axis of the imaging system are presented. When the polarization of the incident light is not perfectly circular, but elliptical, these rotational properties make it possible to deconvolute the

contributions of circular dichroism from those due to linear dichroism. Also the symmetry relationships between the 16 Mueller elements in the bright-field will be presented. These are obtained for the four different media: (*a*) linearly and circularly isotropic, (*b*) circularly anisotropic, (*c*) linearly anisotropic, and (*d*) linearly and circularly anisotropic. In section IV, expressions for the Mueller matrix elements for the first three media are listed in terms of phenomenological optical coefficients. In section V, limitations on the resolution of the differential imaging process are discussed. The concept of depth of field is formulated and the possibility of carrying out optical sectioning in differential polarization imaging is discussed. Section VI gives a brief summary of the main conclusions of this paper.

II. COMPUTATIONS

A. Programming Strategies and Method

Fig. 1 shows the optical arrangements corresponding to the two ways in which Mueller images of an object can be generated. These are: (*a*) bright-field or transmission imaging (B) and (*b*) dark-field or scattering imaging (D). As discussed in paper I of this series, in the bright-field imaging experiment (B), the lens (L) and detector screen (S) are placed directly behind the object (O), along the same direction as the incident light (labeled *z*-axis in Fig. 1). In this geometry, the light absorbed by the object and the light scattered away from the forward direction are the two main contributions to the Mueller images. In describing the polarization of the incident light, the *x*-axis is chosen as the horizontal direction and the *y*-axis as the vertical direction (Fig. 1).

In the dark-field imaging experiment (D), the incident light propagates along any arbitrary direction other than along the *z*-axis, and the positions of the object and the rest of the imaging train are identical to the bright-field geometry (Fig. 1). The direction of incidence is indicated by the unit vector $\hat{\mathbf{k}}_0$. The state of polarization of the incident fields can be described by arbitrary bases vectors

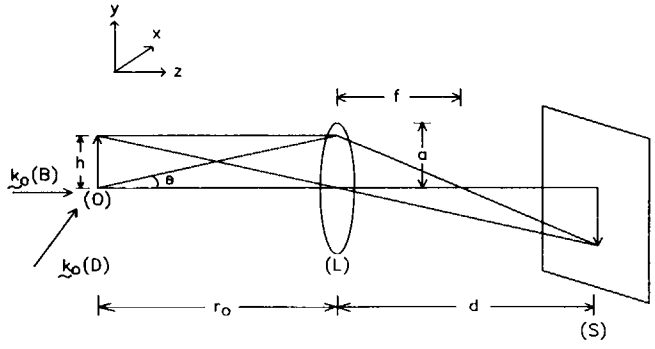

FIGURE 1. Some variables for the calculations of the differential images. The vectors $\hat{\mathbf{k}}_0$ show the direction of the incident light for bright-field (*B*) and dark-field (*D*) imaging.

of a right-handed coordinate system such that

$$\hat{\epsilon}_H = \hat{\epsilon}_V \times \hat{\mathbf{k}}_0,$$

where $\hat{\epsilon}_H$ and $\hat{\epsilon}_V$ are the unit polarization vectors along the horizontal and vertical directions.

Fig. 1 also shows the optical parameters required to perform the numerical computations. These are: the object distance (r_0), the image distance (d), the radius of the lens (a), the focal length (f), the dimension of an object (h), and the wavelength of light (λ). The variables r_0, d, and f are related by the Gaussian lens formula:

$$\frac{1}{r_0} + \frac{1}{d} = \frac{1}{f}.$$

In addition, the paraxial approximation used in the derivation of the theory (see paper I) imposes the condition

$$a + h \ll r_0, \text{ i.e., } a \ll r_0 \text{ and } h \ll r_0,$$

while the thin lens approximation implies that

$$a \ll d.$$

These two restrictions, the paraxial approximation and the thin lens approximation, are included in the theory to ensure minimal alteration of the state of polarization of the light by the lens. Their effect can be seen in the limitations that these approximations impose on the resolution attainable with such an imaging system. The resolution of the optical system was found in paper I to be

$$\Lambda = \frac{0.61\,\lambda_0}{n \sin\theta}.$$

As shown there, for a fixed wavelength of light the optimal resolution is attained by letting $a \to \infty$, then $\Lambda_{opt} = 0.61 \cdot \lambda_0/n$. The resolution for finite apertures is obtained replacing $\sin\theta$ in the above equation by

$$\sin\theta = \frac{a}{(r_0^2 + a^2)^{1/2}}$$

to give

$$\Lambda = \frac{0.61\,\lambda_0}{n}\left(\frac{r_0^2}{a^2} + 1\right)^{1/2}.$$

The above expression shows that, for a fixed wavelength of light, an optical system working under paraxial approximations, ($a \ll r_0$) has a spatial resolution substantially less than the optimal resolution. Thus, the best way to improve the resolution of our imaging system in these calculations is by choosing an appropriately small incident wavelength rather than decreasing the ratio r_0/a. Nonetheless, as mentioned in paper I, in the calculations to be presented here, we have somewhat relaxed this restriction because experimental evidence indicates that the polarization of light is not substantially altered even when using high

numerical aperture objectives. Throughout the computations in this paper, we have used the variables n, r_0, and a in such a way that the optical system has a resolution length between $0.9\,\lambda_0$ and $2.515\,\lambda_0$.

The object is built up of a collection of point polarizable groups located at position $\mathbf{r}_i$. They interact with the incident light by means of a uni-axial polarizability tensor α_i. The coordinates of the point polarizable groups in the object and the directions of the polarizable axes are generated by the computer. This information is then fed into a separate program, which computes the 16 Mueller images. In calculating the Mueller images, the computer first calculates the electric fields or the amplitudes at any position (x, y) on the image plane, using Eqs. 16 and 17 of paper I for the dark-field images and Eq. 29 for the bright-field images. The appropriate unit vectors are substituted into these equations for $\hat{\epsilon}_0$ and $\hat{\epsilon}^0$. The choice of unit vectors depends on which Mueller image is to be generated. The first-order Bessel function appearing in the expression for the tensor, **F**, in these equations, is calculated using the subroutine MMBSJ1 in the IMSL library. The electric fields or amplitudes so obtained are squared to yield the intensity at the point (x, y) on the image plane. The intensities are then added or subtracted point by point according to the formulas given in Table I of paper I. The calculated images are displayed using a DISSPLA contour plotting routine which connects points of equal intensity. Two different contour line types are used: solid lines indicate positive values, whereas dashed lines indicate negative values.

Helices

As an example of the imaging of a chiral structure, we have calculated the dark-field Mueller images of right- and left-handed helices with a radius of $5\,\lambda_0$ and a pitch of $10 \cdot \lambda_0$. Each helix has three complete turns and there are 10 polarizable groups per turn. The polarizability tensor of these groups is assumed to be uniaxial and this axis is oriented tangentially to the line of the helix. The axes of the helices coincide with the y-axis of the laboratory frame (see

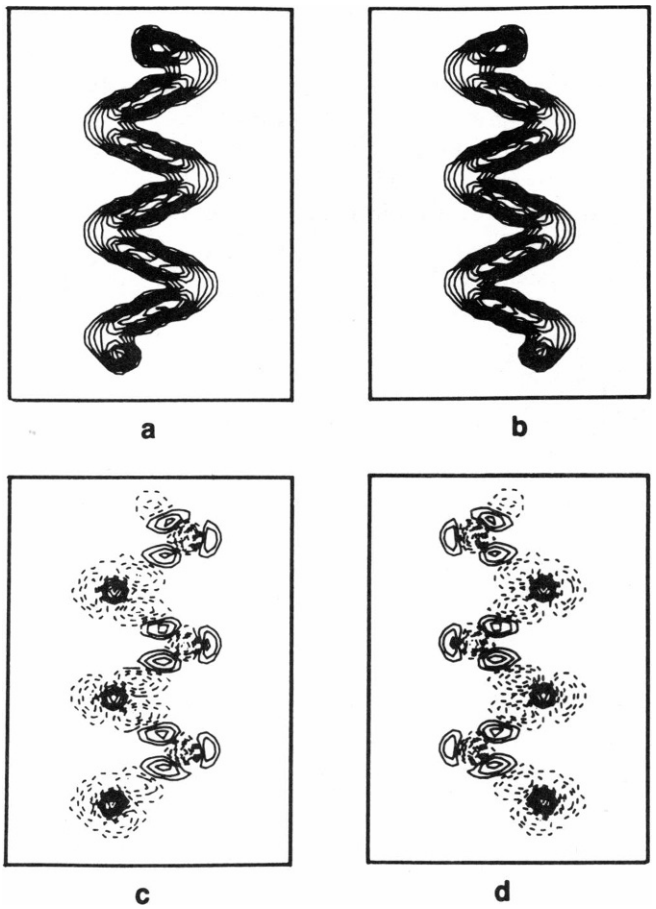

FIGURE 2 M_{11} and M_{44} dark-field images of left- and right-handed helices. (*a*) Normal image (M_{11}) of left-handed helix. (*b*) Normal image (M_{11}) of right-handed helix. (*c*) M_{44} image of left-handed helix. (*d*) M_{44} image of right-handed helix. The maximum intensity of M_{44} (*c* and *d*) is ~0.29 times as large as the total image intensity (M_{11}). Solid contours indicate positive intensities, whereas dashed contours indicate negative intensities.

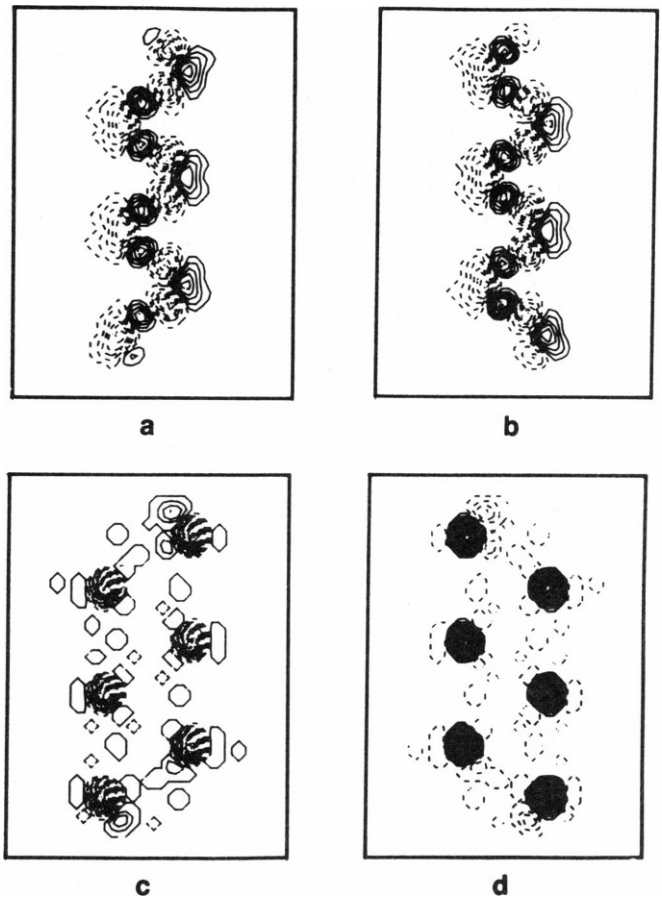

FIGURE 3 M_{14} and M_{41} dark-field images of left- and right-handed helices. (*a*) M_{14} image of left-handed helix. (*b*) M_{14} image of right-handed helix. (*c*) M_{41} image of left-handed helix. (*d*) M_{41} image of right-handed helix. The positive maximum intensities of M_{14} (*a* and *b*) and M_{41} (*c* and *d*) and ~0.3 and 0.38 times as large as the total image intensity (M_{11}), respectively.

Fig. 1) and the incident light propagates along this direction from the negative to the positive y-axis. The lens is placed at a distance $d = 667\ \lambda_0$ from the object. The plane of the lens is perpendicular to the z-axis of the laboratory frame so that the main contribution to the images is provided by light scattered at 90°. The z- and x-axes are chosen as the incident horizontal and vertical directions, respectively. The resolution length Λ is chosen to be $2.74 \cdot \lambda_0$. Fig. 2 shows the unnormalized M_{11} (*top row*) and M_{44} (*bottom row*) images of the right-handed (*right column*) and left-handed (*left column*) helices. The M_{11} images, obtained using unpolarized light, display only positive values (continuous lines), whereas the M_{44} images show alternating lobes of positive and negative regions. Although the M_{11} and M_{44} images of the opposite-handed objects appear as mirror images of each other in space, the sign of each domain in the image remains unchanged with reversal of the handedness. Thus, these Mueller images are not sensitive to the chiral nature of the object. Fig. 3 depicts the M_{14} (*top row*) and M_{41} (*bottom row*) images of these same right-handed (*right column*) and left-handed (*left column*) helices. In this case the images are sensitive to the chirality of the objects, for the images of opposite-handed helices are mirror images of each other both in shape and sign. In general the rest of the dark-field Mueller images depend on the imaging geometry (or the scattering direction) and are not shown here.

Differential Polarization Imaging of Metaphase Chromosomes

Organization. During the last ten years the basic structure of chromatin has been unraveled. Chromatin appears to be organized in hierarchical structures in

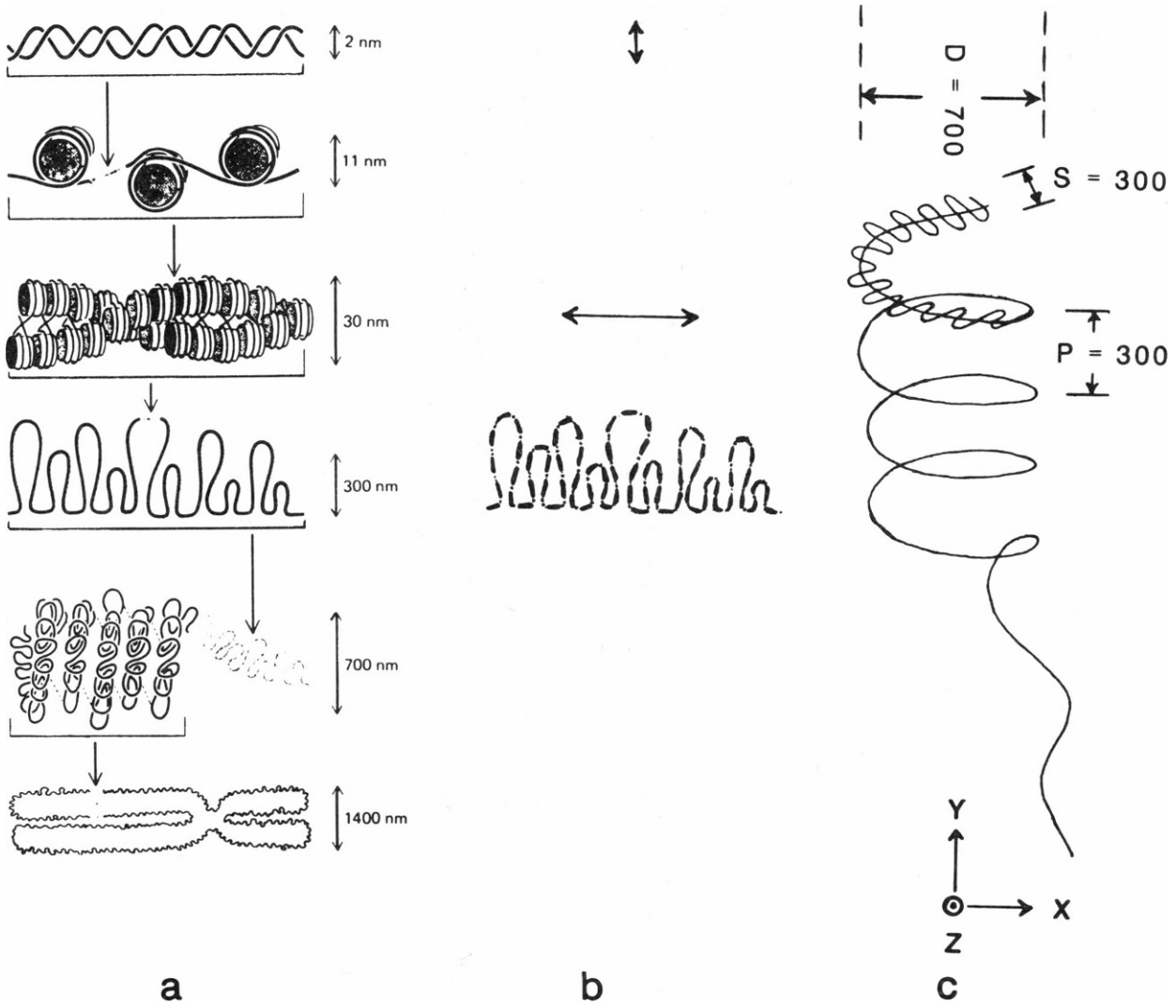

FIGURE 4 Schematic illustration of the different orders of chromatin packing postulated to give rise to the highly condensed metaphase chromosome (*a;* reproduced from Molecular Biology of the Cell, 1983, Garland Publishing Inc., New York, 399), the orientation of the transition dipole moments for the hierarchichal orders of organization (*b*), and the dimensions of the model chromosome (left-handed helix superimposed with a sinewave) (*c*). The helix axis is along the y-axis, the incident light propagates along $+x$-axis, and the screen is on the $+z$-axis.

which the lower level organization is maintained through the higher-order coiling. Fig. 4 *a* shows the successive orders of organization starting with the isolated DNA molecule. Next is the nucleosome structure which is now well-established (4–7), as well as the 10-nm "beads-on-a-string" fiber (9–12). The next level of the chromatin structure corresponds to a coiling of the 10-nm fiber into a shallow solenoid 30 nm in diameter with six nucleosomes per turn (13–15). The detailed path of the linker DNA in between nucleosomes and the precise location of histone H1 are still a matter of controversy (16–19), but most models agree in their main features. The next level of organization, both in interphase nuclei and in metaphase chromosomes, appears to be a folding of the 30-nm fiber into loops (20) or domains anchored to a scaffold by specific non-histone proteins (21, 22). These loops are 35–100 kilobase pairs long. Their organization into higher order structures is a subject of active research (23, 24). A radial organization of the loops around a metallo-protein scaffold has been proposed (25); additional levels of spiralization (26) and a side by side association of the loops have also been suggested (24, 27).

The Model. To model this complex structure we must necessarily simplify many of the details described above. Nonetheless, the resulting model must preserve the essential features of the structure, in particular with regard to the orientation of its transition dipole moments. Our choice can be seen in Fig. 4 *b*, where the direction of the dipoles is indicated through the different hierarchical orders of organization. DNA is a highly dichroic molecule and its transition moments in the UV are all in the base planes and perpendicular to the helix axis. As shown in Fig. 4 *b*, this orientation is inverted at the level of the 30-nm diam solenoid. This solenoidal structure is then arranged in loops on which the transition dipoles are tangentially oriented. This looped structure is then coiled into a 700-nm diam helix. In the model, the point polarizable groups are arranged to form the looped structure. The polarizability tensor at each group is assumed to be uni-axial and tangential at every point in the loop. The loop itself is modeled as a sinusoidal curve with a peak-to-peak amplitude of 300 nm. This sinusoidal curve coils into a 700-nm diam helix so that the loops are arranged radially on the helix. There are twelve loops per turn of the helix. Since each loop is built with eight polarizable groups, each group represents a large number of DNA base pairs. The dimensions used in the model (expressed in nanometers) are shown in Fig. 4 *c*.

Dark-field Imaging of the Chromosome Model. Fig. 5 shows the dark-field images obtained for the chromosome model described above. The wavelength of the incident light (λ_0) is 200 nm and the aperture of the lens is 100 λ_0. The refractive index n is 1.5 and the resolution length Λ is 0.9 λ_0. The incident light propagates

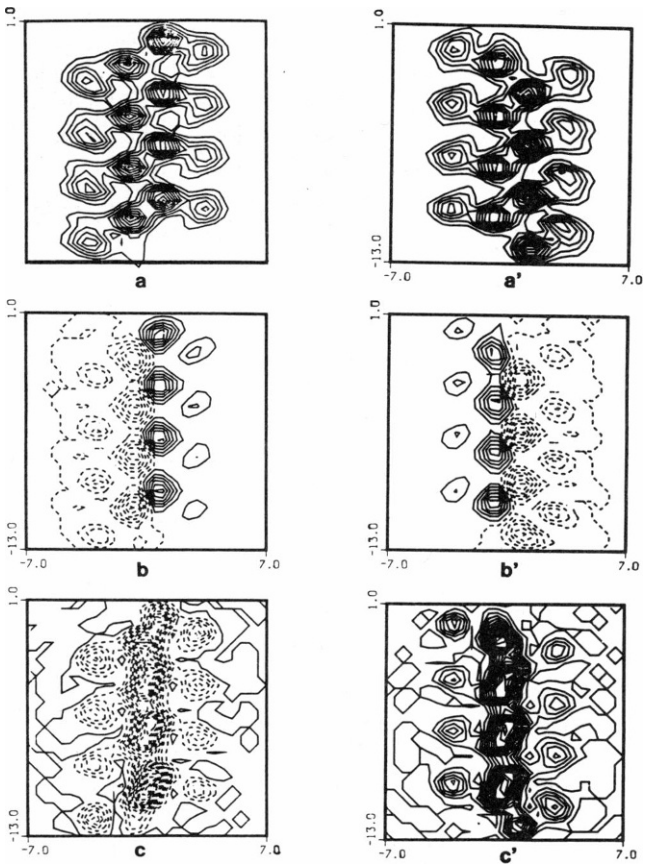

FIGURE 5 M_{11} (*a* and *a'*), M_{13} (*b* and *b'*) and M_{14} (*c* and *c'*) images for left- (*left column*) and right-handed (*right column*) helices. The model of the left-handed helix is drawn in Fig. 4 *c*.

along the *x*-axis and the optical axis of the lens is aligned along the *z*-axis of the laboratory frame. In the left-hand column, *a*, *b*, and *c* represent the unnormalized M_{11}, M_{13}, and M_{14} images of a four-turn segment of the 700-nm diam left-handed helix. The right column depicts these same Mueller images for a right-handed helix. As in the case of the helix models shown in Fig. 2, the M_{11} images (Fig. 5, *a* and *a'*) appear as mirror images of each other only in shape, while the M_{13} and M_{14} images (Fig. 5, *b'*, *c*, and *c'*) are mirror images both in shape and sign. With this specific model, the M_{13} images (Fig. 5, *b* and *b'*) for left- and right-handed helices have their signs interchanged. However, this does not happen in all cases, but depends on the direction of vibration of the incident light and the details of the structure of the helix (especially on how the sinusoidal curve coils into a 700-nm diam helix). The M_{14} image in this model displays only negative values for the left-handed helix (Fig. 5 *c*) and positive for the right-handed helix (Fig. 5 *c'*). The detailed features of the M_{14} images again depend on the details of the 700-nm diam helix. However, because M_{14} images are sensitive to the chirality of the object, M_{14} images for helices with opposite handedness always show opposite signs regardless of the detailed structure of the helices. Fig. 5 indicates that differential polarization imaging of metaphase chromo-

somes might provide sufficient structural details to test alternative models for the long-range organization. We have found that the details of the calculated images are highly sensitive to the model chosen for the coiling of the looped structures along the 700-nm diam helix (results not shown here). This appears as a clear indication of the possibility of applying this technique to elucidate these complex molecular organizations.

III. SYMMETRY PROPERTIES OF THE MUELLER IMAGES

A. Infinitesimal Rotations

In this section, we will investigate the symmetry properties of the Mueller matrix elements and the relationships among them. Here we make use of the fact that the form of the expressions derived and presented in paper I of this series should remain unchanged after an infinitesimal rotation of the laboratory frame about the axes defined by the direction of incidence of the light and the direction perpendicular to the imaging plane. This property, a consequence of the isotropy of space (28), assures that the relations to be obtained will be of a general nature and independent of the details of the object. Furthermore, this treatment is valid for both bright- and dark-field imaging geometries, and both will be carried out simultaneously.

In regular polarization spectroscopy, a rotation of the laboratory frame can be carried out in either of two ways: (*a*) by rotating the object while the analyzer and polarizer axes are held fixed, or (*b*) keeping the object fixed while rotating the analyzer and polarizer directions. However, these two schemes are not equivalent in an experiment in which the signals are to be space-resolved (imaged) in the detector plane. In this case, it is desirable to keep the orientation of the object unaltered. Thus we will use procedure (*b*), keeping in mind that the results of this treatment will be valid in those cases in which the spectroscopic signals are not spatially resolved.

Fig. 6 shows two right-handed coordinate systems labeled $\hat{\epsilon}_H$, $\hat{\epsilon}_V$, and $\hat{k}_0$ for the incident light, and labeled $\hat{\epsilon}^H$, $\hat{\epsilon}^V$, and $\hat{z}$ for the transmitted light. The operation to be performed is the simultaneous rotation of two coordinate systems about the $\hat{k}_0$ and $\hat{z}$ directions. After a positive rotation by an angle $d\theta$ (counterclockwise when seen by the observers in Fig. 6), the frame will be in the primed position depicted by the dotted lines. The relationships between the primed and unprimed axes are (29)

$$\begin{aligned}\hat{\epsilon}'_H &= \hat{\epsilon}_H + (\hat{k}_0 \times \hat{\epsilon}_H)d\theta = \hat{\epsilon}_H + \hat{\epsilon}_V d\theta \\ \hat{\epsilon}'_V &= \hat{\epsilon}_V + (\hat{k}_0 \times \hat{\epsilon}_V)d\theta = \hat{\epsilon}_V - \hat{\epsilon}_H d\theta \\ \hat{k}'_0 &= \hat{k}_0. \end{aligned} \quad (1)$$

To investigate the behavior of the Mueller matrix elements under this transformation, we simply substitute these relationships into the expressions for the Mueller entries in

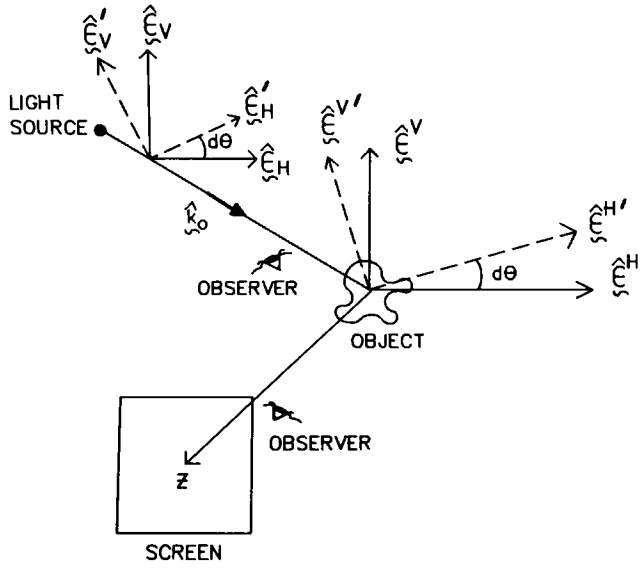

FIGURE 6 An infinitesimal rotation about $\hat{k}_0$ and the z-axis. $d\theta$ is positive when the rotation is performed counterclockwise.

Table I. The behavior of the matrix elements upon this transformation can be separated into three distinct classes as shown below.

Class I: $M_{11}, M_{14}, M_{41}, M_{44}$. Careful inspection of these entries shows that they are all invariant to an infinitesimal rotation about the incident ($\hat{k}_0$) and transmitted ($\hat{z}$) directions. For these elements, these axes behave as C_∞ symmetry axes. Thus, these terms can be grouped into a class of terms consisting of all the Mueller matrix elements that are invariant under rotations.

TABLE I

$$\begin{aligned}
M_{11} &= A\,\Gamma_{\alpha\beta}(1 - \hat{k}_0\hat{k}_0)_{\alpha\beta} \\
M_{12} &= A\,\Gamma_{\alpha\beta}(\hat{\epsilon}_{H\alpha}\hat{\epsilon}_{H\beta} - \hat{\epsilon}_{V\alpha}\hat{\epsilon}_{V\beta}) \\
M_{13} &= A\,\Gamma_{\alpha\beta}(\hat{\epsilon}_{H\alpha}\hat{\epsilon}_{V\beta} + \hat{\epsilon}_{V\alpha}\hat{\epsilon}_{H\beta}) \\
M_{21} &= A(\hat{r}\cdot\hat{z})^2[Q\dagger\cdot(\hat{\epsilon}^H\hat{\epsilon}^H - \hat{\epsilon}^V\hat{\epsilon}^V)\cdot Q]_{\alpha\beta}(1 - \hat{k}_0\hat{k}_0)_{\alpha\beta} \\
M_{31} &= A(\hat{r}\cdot\hat{z})^2[Q\dagger\cdot(\hat{\epsilon}^H\hat{\epsilon}^V + \hat{\epsilon}^V\hat{\epsilon}^H)\cdot Q]_{\alpha\beta}(1 - \hat{k}_0\hat{k}_0)_{\alpha\beta} \\
M_{22} &= A(\hat{r}\cdot\hat{z})^2[Q\dagger\cdot(\hat{\epsilon}^H\hat{\epsilon}^H - \hat{\epsilon}^V\hat{\epsilon}^V)\cdot Q]_{\alpha\beta}(\hat{\epsilon}_{H\alpha}\hat{\epsilon}_{H\beta} - \hat{\epsilon}_{V\alpha}\hat{\epsilon}_{V\beta}) \\
M_{23} &= A(\hat{r}\cdot\hat{z})^2[Q\dagger\cdot(\hat{\epsilon}^H\hat{\epsilon}^H - \hat{\epsilon}^V\hat{\epsilon}^V)\cdot Q]_{\alpha\beta}(\hat{\epsilon}_{H\alpha}\hat{\epsilon}_{V\beta} + \hat{\epsilon}_{V\alpha}\hat{\epsilon}_{H\beta}) \\
M_{32} &= A(\hat{r}\cdot\hat{z})^2[Q\dagger\cdot(\hat{\epsilon}^H\hat{\epsilon}^V + \hat{\epsilon}^V\hat{\epsilon}^H)\cdot Q]_{\alpha\beta}(\hat{\epsilon}_{H\alpha}\hat{\epsilon}_{H\beta} - \hat{\epsilon}_{V\alpha}\hat{\epsilon}_{V\beta}) \\
M_{33} &= A(\hat{r}\cdot\hat{z})^2[Q\dagger\cdot(\hat{\epsilon}^H\hat{\epsilon}^V + \hat{\epsilon}^V\hat{\epsilon}^H)\cdot Q]_{\alpha\beta}(\hat{\epsilon}_{H\alpha}\hat{\epsilon}_{V\beta} + \hat{\epsilon}_{V\alpha}\hat{\epsilon}_{H\beta}) \\
M_{14} &= -i\,\Lambda_{\alpha\beta\gamma}L_{\omega\gamma}(\hat{\epsilon}_R \times \hat{\epsilon}_L)_\beta \equiv -i\,\Lambda_{\alpha\beta\gamma}L_{\omega\gamma}\hat{k}_{0\beta} \\
M_{24} &= -i(\hat{r}\cdot\hat{z})^2\Lambda_{\alpha\beta\gamma}(\hat{\epsilon}^H_\alpha\hat{\epsilon}^H_\gamma - \hat{\epsilon}^V_\alpha\hat{\epsilon}^V_\gamma)\hat{k}_{0\beta} \\
M_{34} &= -i(\hat{r}\cdot\hat{z})^2\Lambda_{\alpha\beta\gamma}(\hat{\epsilon}^H_\alpha\hat{\epsilon}^V_\gamma + \hat{\epsilon}^V_\alpha\hat{\epsilon}^H_\gamma)\hat{k}_{0\beta} \\
M_{44} &= (\hat{r}\cdot\hat{z})^2\Lambda_{\alpha\beta\gamma}[(1\times 1)\cdot\hat{z}]_{\alpha\gamma}\hat{k}_{0\beta} \\
M_{41} &= -i(\hat{r}\cdot\hat{z})^2\Lambda^\dagger_{\alpha\beta\gamma}(1 - \hat{k}_0\hat{k}_0)_{\alpha\gamma}\hat{z}_\beta \\
M_{42} &= -i(\hat{r}\cdot\hat{z})^2\Lambda^\dagger_{\alpha\beta\gamma}(\hat{\epsilon}_{H\alpha}\hat{\epsilon}_{H\gamma} - \hat{\epsilon}_{V\alpha}\hat{\epsilon}_{V\gamma})\hat{z}_\beta \\
M_{43} &= -i(\hat{r}\cdot\hat{z})^2\Lambda^\dagger_{\alpha\beta\gamma}(\hat{\epsilon}_{H\alpha}\hat{\epsilon}_{V\gamma} + \hat{\epsilon}_{V\alpha}\hat{\epsilon}_{H\gamma})\hat{z}_\beta
\end{aligned}$$

with

$$\Gamma \equiv Q\dagger\cdot L\cdot Q$$

and

$$L = (\hat{r}\cdot\hat{z})^2 1 - (\hat{r}\cdot\hat{z})(\hat{r}\hat{z} + \hat{z}\hat{r}) + \hat{r}\hat{r}.$$

Also

$$\Lambda_{\alpha\beta\gamma} \equiv A(Q\times Q\dagger)_{\alpha\beta\gamma},$$

where A is a real constant, and $Q = F$ for dark-field and $Q = G$ for bright-field, in the notation of the paper I of this series.

Class II: M_{12}, M_{13}, M_{21}, M_{31}, M_{42}, M_{43}, M_{24}, M_{34}. Analysis of this class will be carried out only for the elements M_{12} and M_{13}, and we will give the results for the other elements in this class.

Upon an infinitesimal rotation, M_{12} transforms according to

$$M'_{12} = A\{\mathbf{Q}\dagger \cdot [(\hat{\mathbf{r}} \cdot \hat{\mathbf{z}})^2 \mathbf{1} - (\hat{\mathbf{r}} \cdot \hat{\mathbf{z}})(\hat{\mathbf{z}}\hat{\mathbf{r}} + \hat{\mathbf{r}}\hat{\mathbf{z}}) + \hat{\mathbf{r}}\hat{\mathbf{r}}] \cdot \mathbf{Q}\}_{\alpha\beta} \cdot (\hat{\epsilon}'_{H\alpha}\hat{\epsilon}'_{H\beta} - \hat{\epsilon}'_{V\alpha}\hat{\epsilon}'_{V\beta}). \quad (2)$$

Substituting Eqs. 1 into 2 we have

$$M'_{12} = M_{13}(\theta + d\theta) = M_{12}(\theta) + 2M_{13}(\theta)\, d\theta, \quad (3)$$

where the definitions of M_{12} and M_{13} in Table I have been used. In the limit when $d\theta \rightarrow 0$:

$$\frac{dM_{12}(\theta)}{d\theta} = 2M_{13}(\theta). \quad (4)$$

Thus we have arrived at a differential relationship between two elements of the Mueller matrix. Next, we investigate the effect of the transformation on M_{13}. After an infinitesimal rotation, M_{13} becomes

$$M'_{13} = A\{\mathbf{Q}\dagger \cdot [(\hat{\mathbf{r}} \cdot \hat{\mathbf{z}})^2 \mathbf{1} - (\hat{\mathbf{r}} \cdot \hat{\mathbf{z}})(\hat{\mathbf{z}}\hat{\mathbf{r}} + \hat{\mathbf{r}}\hat{\mathbf{z}}) + \hat{\mathbf{r}}\hat{\mathbf{r}}] \cdot \mathbf{Q}\}_{\alpha\beta} \cdot (\hat{\epsilon}'_{H\alpha}\hat{\epsilon}'_{V\beta} + \hat{\epsilon}'_{V\alpha}\hat{\epsilon}'_{H\beta}).$$

Again, using Eqs. 1 we obtain

$$M'_{13} = M_{13}(\theta + d\theta) = M_{13}(\theta) - 2M_{12}(\theta)\, d\theta$$

and in the limit $d\theta \rightarrow 0$:

$$\frac{dM_{13}(\theta)}{d\theta} = -2M_{12}(\theta). \quad (5)$$

Eqs. 4 and 5 can be combined into one second-order differential equation:

$$\frac{d^2M_{12}(\theta)}{d\theta^2} = -4M_{12}(\theta). \quad (6)$$

The most general solution to this differential equation is

$$M_{12}(\theta) = Ae^{2i\theta} + Be^{-2i\theta}.$$

The coefficients A and B can be obtained from the appropriate initial conditions:

$$M_{12}(\theta = 0) = M_{12}(0) = A + B$$

and

$$\left.\frac{dM_{12}}{d\theta}\right|_{\theta=0} = 2M_{13}(0) = 2i(A - B)$$

to yield the desired relation

$$M_{12}(\theta) = M_{12}(0)\cos 2\theta + M_{13}(0)\sin 2\theta. \quad (7)$$

Similarly, from Eq. 5 and the above relation, we have

$$M_{13}(\theta) = M_{13}(0) - 2\int_0^\theta [M_{12}(0)\cos 2\theta + M_{13}(0)\sin 2\theta]\, d\theta$$

$$M_{13}(\theta) = M_{13}(0)\cos 2\theta - M_{12}(0)\sin 2\theta. \quad (8)$$

Eqs. 7 and 8 are the two final expressions. It can be seen that they can be combined to give a single expression relating $M_{12}(\theta)$ and $M_{13}(\theta)$. More importantly, they determine the symmetry behavior of these elements upon rotation about the $\hat{\mathbf{k}}_0$ direction. Further discussion of this point will be deferred until later.

The derivation of the relationships for all other terms in this class is identical and need not be repeated here.

Class III: M_{22}, M_{33}, M_{23}, and M_{32}. After infinitesimal rotation of the polarizer and analyzer axes, M_{22} becomes

$$M'_{22} = A(\hat{\mathbf{r}} \cdot \hat{\mathbf{z}})^2[\mathbf{Q}\dagger \cdot (\hat{\epsilon}'^{H}\hat{\epsilon}'^{H} - \hat{\epsilon}'^{V}\hat{\epsilon}'^{V}) \cdot \mathbf{Q}]_{\alpha\beta} \cdot (\hat{\epsilon}'_{H\alpha}\hat{\epsilon}'_{H\beta} - \hat{\epsilon}'_{V\alpha}\hat{\epsilon}'_{V\beta}).$$

Substituting Eqs. 1 into this expression, we obtain

$$M'_{22} - M_{22} = 2(M_{32} + M_{23})$$

and in the limit as $d\theta \rightarrow 0$:

$$\frac{dM_{22}}{d\theta} = 2(M_{32} + M_{23}). \quad (9)$$

Similarly we can obtain

$$\frac{dM_{32}}{d\theta} = 2(M_{33} - M_{22}) \quad (10)$$

and

$$\frac{dM_{33}}{d\theta} = -2(M_{32} + M_{23}) \quad (11)$$

and

$$\frac{dM_{23}}{d\theta} = 2(M_{33} - M_{22}). \quad (12)$$

These four first-order differential equations can be combined to yield two second-order equations:

$$\frac{d^2M_{22}}{d\theta^2} = -8(M_{22} - M_{33})$$

$$\frac{d^2M_{33}}{d\theta^2} = 8(M_{22} - M_{33}). \quad (13)$$

An alternative choice of variables yields

$$\frac{d^2M_{32}}{d\theta^2} = -8(M_{32} + M_{23})$$

and

$$\frac{d^2M_{23}}{d\theta^2} = -8\,(M_{32} + M_{23}). \tag{14}$$

Subtracting the pair of Eqs. 13 and adding the pair of Eqs. 14, we obtain

$$\frac{d^2(M_{22} - M_{33})}{d\theta^2} = -16\,(M_{22} - M_{33})$$

$$\frac{d^2(M_{23} + M_{32})}{d\theta^2} = -16\,(M_{23} + M_{32}).$$

These two equations can be integrated using appropriate boundary conditions giving

$$M_{22}(\theta) - M_{33}(\theta) = [M_{22}(0) - M_{33}(0)]\cos 4\theta + [M_{32}(0) + M_{23}(0)]\sin 4\theta$$

and

$$M_{23}(\theta) + M_{32}(\theta) = [M_{23}(0) + M_{32}(0)]\cos 4\theta + [M_{33}(0) - M_{22}(0)]\sin 4\theta.$$

The solutions for $M_{22}(\theta)$ and $M_{33}(\theta)$ can be separated by using the fact that (see Eqs. 9–12):

$$M_{22}(\theta) + M_{33}(\theta) = \text{constant} = M_{22}(0) + M_{33}(0)$$

and

$$M_{23}(\theta) - M_{32}(\theta) = \text{constant} = M_{23}(0) - M_{32}(0).$$

Using these expressions we finally obtain

$$\begin{aligned}
M_{22}(\theta) &= -\tfrac{1}{2}[M_{33}(0) - M_{22}(0)]\cos 4\theta + \tfrac{1}{2}[M_{32}(0) + M_{23}(0)]\sin 4\theta + \tfrac{1}{2}[M_{22}(0) + M_{33}(0)]\\
M_{33}(\theta) &= \tfrac{1}{2}[M_{33}(0) - M_{22}(0)]\cos 4\theta - \tfrac{1}{2}[M_{32}(0) + M_{23}(0)]\sin 4\theta + \tfrac{1}{2}[M_{22}(0) + M_{33}(0)]\\
M_{23}(\theta) &= \tfrac{1}{2}[M_{23}(0) + M_{32}(0)]\cos 4\theta + \tfrac{1}{2}[M_{33}(0) - M_{22}(0)]\sin 4\theta + \tfrac{1}{2}[M_{23}(0) - M_{32}(0)]\\
M_{32}(\theta) &= \tfrac{1}{2}[M_{23}(0) + M_{32}(0)]\cos 4\theta + \tfrac{1}{2}[M_{33}(0) - M_{22}(0)]\sin 4\theta - \tfrac{1}{2}[M_{23}(0) - M_{32}(0)].
\end{aligned}$$

The derivation of these relationships among the elements of the Mueller matrix leads to a number of interesting conclusions regarding their symmetry properties. First it is seen that sixteen differential relations among the Mueller elements can be obtained. This permits the definition of the derivative Mueller matrix depicted in Fig. 7. Notice that the derivative matrix has a zero trace and that the elements

$\frac{dM}{d\theta} =$

0	$2M_{13}$ ⟷ $-2M_{12}$		0
$2M_{31}$ ↕	$2(M_{23}+M_{32})$ ⤡⤢	$2(M_{33}-M_{22})$	$2M_{34}$ ↕
$-2M_{21}$ ↕	$2(M_{33}-M_{22})$	$-2(M_{23}+M_{32})$	$-2M_{24}$ ↕
0	$2M_{43}$ ⟷ $-2M_{42}$		0

FIGURE 7 The first derivatives of the Mueller matrix elements.

in the four corners vanish, corresponding to the class of invariant elements in the Mueller matrix. Furthermore, this derivative matrix is symmetric in the sense that the relationships below the diagonal can be obtained from those above the diagonal by simply exchanging the subindices. The differential relations are connected in pairs, as indicated in Fig. 7 by the double-headed arrows. This pairing of the Mueller elements leads to the derivation of second-order differential equations. Integration of the second-order differential equations then leads to the sixteen relationships describing the symmetry behavior of each of the Mueller elements upon a rotation of the polarizer and analyzer axes. These relationships are shown in Table II

TABLE II

Class I: Totally symmetric (invariant)

$$M_{ij}(\theta) = M_{ij}(0), \quad (i, j = 1, 4).$$

Class II: Twofold symmetric

$$\left.\begin{aligned} M_{ij}(\theta) &= M_{ij}(0)\cos 2\theta \pm M_{ij\pm 1}(0)\sin 2\theta \\ M_{ji}(\theta) &= M_{ji}(0)\cos 2\theta \pm M_{j\pm 1,i}(0)\sin 2\theta \end{aligned}\right\} (i = 1, 4 \text{ and } j = 2, 3)$$

+ if j is even, and − if j is odd.

Class III: Pseudo-fourfold symmetric

$$\begin{aligned}
M_{22}(\theta) &= -\frac{1}{2}[M_{33}(0) - M_{22}(0)]\cos 4\theta + \frac{1}{2}[M_{32}(0) + M_{23}(0)]\sin 4\theta + \frac{1}{2}[M_{22}(0) + M_{33}(0)]\\
M_{33}(\theta) &= \frac{1}{2}[M_{33}(0) - M_{22}(0)]\cos 4\theta - \frac{1}{2}[M_{32}(0) + M_{23}(0)]\sin 4\theta + \frac{1}{2}[M_{22}(0) + M_{33}(0)]\\
M_{23}(\theta) &= \frac{1}{2}[M_{23}(0) + M_{32}(0)]\cos 4\theta + \frac{1}{2}[M_{33}(0) - M_{22}(0)]\sin 4\theta + \frac{1}{2}[M_{23}(0) - M_{32}(0)]\\
M_{32}(\theta) &= \frac{1}{2}[M_{23}(0) + M_{32}(0)]\cos 4\theta + \frac{1}{2}[M_{33}(0) - M_{22}(0)]\sin 4\theta - \frac{1}{2}[M_{23}(0) - M_{32}(0)].
\end{aligned}$$

where the Mueller elements have been classified into three main classes according to their symmetry behavior. The first class corresponds to the elements invariant under rotations. Class II includes eight elements that display a twofold symmetry under rotation. These elements change sign upon a rotation of $\pi/2$ radians and reproduce themselves after a rotation of π radians. These elements are seen to be the sum of an element which is even (symmetric) in the rotation angle and an element which is odd (antisymmetric). Class III consists of four elements that contain a fourfold symmetric contribution as well as a term invariant upon rotation. These elements do not change sign upon a rotation of $\pi/4$ radians, although they reproduce themselves after $\pi/2$ radians. For this reason, this class is referred to as pseudo fourfold symmetric.

It should be emphasized that these relationships are completely general and independent of whether an imaging element (lens) is placed in the optical train or not. Moreover, the derivation is also independent of the description of the light-matter interaction event and is therefore valid for all-order Born-Approximations of the fields.

B. Application of the Rotational Symmetry: Imaging with Imperfect Circular Polarizations

The quality of the incident circular polarizations is an essential consideration when obtaining M_{i4} $(i = 1, 2, 3, 4)$ Mueller images, since any imperfections in the incident circular polarizations will give rise to spurious linear artifacts in the Mueller images. In this section, we analyze these artifacts and show how to eliminate them by using the symmetry properties discussed in the previous section. To separate the Mueller images from linear polarization artifacts, the Mueller images must be invariant upon a rotation of the optical components of the imaging system. Since only M_{14} and M_{44}, among M_{i4} $(i = 1, 2, 3, 4)$, satisfy this requirement, we present an analysis only of these two Mueller images.

The theoretical analysis is carried out by replacing the incident circular polarization vectors in the expressions for M_{14} and M_{44} of Table I, by unit vectors representing right- $(\hat{\epsilon}_+)$ or left- $(\hat{\epsilon}_-)$ elliptically polarized light, which are written as

$$\hat{\epsilon}_+ = \cos\delta_+ \, e^{-i\phi_+} \, \hat{\epsilon}_R + \sin\delta_+ \, e^{i\phi_+} \, \hat{\epsilon}_L \tag{15}$$

$$\hat{\epsilon}_- = \sin\delta_- \, e^{-i\phi_-} \, \hat{\epsilon}_R + \cos\delta_- \, e^{i\phi_-} \, \hat{\epsilon}_L \tag{16}$$

where $\hat{\epsilon}_R$ and $\hat{\epsilon}_L$ represent pure right- and left-circular polarizations. $\delta_\pm$ gives the ellipticities of $\hat{\epsilon}_\pm$, and $\phi_\pm$ are the angles of inclination of $\hat{\epsilon}_\pm$. After some algebra, we obtain

$$\begin{aligned} M'_{14} = {} & \tfrac{1}{2}(\cos 2\delta_+ + \cos 2\delta_-) M_{14} \\ & + \tfrac{1}{2}(\alpha_+ \cos 2\phi_+ - \alpha_- \cos 2\phi_-) M_{12} \\ & + \tfrac{1}{2}(\alpha_+ \sin 2\phi_+ - \alpha_- \sin 2\phi_-) M_{13} \end{aligned} \tag{17}$$

$$\begin{aligned} M'_{44} = {} & \tfrac{1}{2}(\cos 2\delta_+ + \cos 2\delta_-) M_{44} \\ & + \tfrac{1}{2}(\alpha_+ \cos 2\phi_+ - \alpha_- \cos 2\phi_-) M_{42} \\ & + \tfrac{1}{2}(\alpha_+ \sin 2\phi_+ - \alpha_- \sin 2\phi_-) M_{43}, \end{aligned} \tag{18}$$

where the prime indicates that the Mueller images have been formed using imperfect incident circular polarizations, and the unprimed Mueller elements indicate those images obtained using pure circular or pure linear polarizations of the incident light. $\alpha_\pm$ are the fractional ellipticities of $\hat{\epsilon}_\pm$, which are defined as

$$\alpha_\pm = \frac{u_\pm^2 - v_\pm^2}{u_\pm^2 + v_\pm^2} = \sin 2\delta_\pm,$$

where $u_\pm$ and $v_\pm$ are the lengths of the major and the minor axis of $\hat{\epsilon}_\pm$, respectively. $\cos 2\delta_\pm$, appearing in Eqs. 17 and 18, can be expressed in terms of the fractional ellipticities $\alpha_\pm$ (which are always small under experimental conditions) as

$$\cos 2\delta_\pm = (1 - \alpha_\pm^2)^{1/2}.$$

If we expand this equation to first-order in $\alpha_\pm$ and substitute it into Eqs. 17 and 18, we obtain

$$\begin{aligned} M'_{14} = {} & M_{14} + \tfrac{1}{2}(\alpha_+ \cos 2\phi_+ - \alpha_- \cos 2\phi_-) M_{12} \\ & + \tfrac{1}{2}(\alpha_+ \sin 2\phi_+ - \alpha_- \sin 2\phi_-) M_{13} \end{aligned} \tag{19}$$

$$\begin{aligned} M'_{44} = {} & M_{44} + \tfrac{1}{2}(\alpha_+ \cos 2\phi_+ - \alpha_- \cos 2\phi_-) M_{42} \\ & + \tfrac{1}{2}(\alpha_+ \sin 2\phi_+ - \alpha_- \sin 2\phi_-) M_{43}. \end{aligned} \tag{20}$$

For simplicity, the above equations are not normalized. Notice that in the case of imperfect circular polarizations, M'_{i4} $(i = 1, 4)$ contains the true M_{i4} mixed with the contributions from M_{i2} and M_{i3}. This mixing is proportional to the difference in ellipticities between the two incident polarizations $(\alpha_\pm)$ and their inclination angles $(\phi_\pm)$. As expected, when the incident polarizations are purely circular, $\alpha_\pm = 0$ and only M_{i4} remains. Similarly, if the two incident polarizations have the same ellipticity and the same orientation the coefficients

$$S = \tfrac{1}{2}(\alpha_+ \cos 2\phi_+ - \alpha_- \cos 2\phi_-)$$

and

$$T = \tfrac{1}{2}(\alpha_+ \sin 2\phi_+ - \alpha_- \sin 2\phi_-)$$

vanish identically and only the pure M_{i4} term contributes. The double-angle dependence appearing in these coefficients assures that if the incident polarizations have the same ellipticity but supplementary inclinations, i.e., $\phi_- = 180 - \phi_+$, the coefficient of M_{i2} vanishes but not that of M_{i3}. This is due to the oriented nature of the anisotropic object. Eqs. 19 and 20 also show that the mixing of Mueller element contributions to the image is linear.

Notice that the M_{i2} and M_{i3} elements are twofold symmetric with respect to rotations about the optical axis, while the elements M_{i4} $(i = 1, 4)$ are invariant under this

operation, as was shown in the previous section. Furthermore, the M_{i2} and M_{i3} ($i = 1, 4$) contributions change sign upon a $\pi/2$ rotation about the optical axis. Therefore, rotating the optical components (polarizers, retarders, and analyzers) by an angle of $\pi/2$ radians about this axis, permits us to cancel out the contributions from the M_{i2} and M_{i3} images:

$$\frac{M'_{i4}\left(\theta + \frac{\pi}{2}\right) + M'_{i4}(\theta)}{2} = M_{i4}(\theta) = M_{i4}.$$

This simple result allows us to de-convolute the linear contributions from the circular polarization preference exhibited by a chiral sample.

Again, since this method uses the results from the previous section on the rotational symmetry properties, it is valid for all Born-Approximations and does not depend on the optical thickness of the sample. As discussed in paper I, the M_{14} image for an optically thin sample in the first Born-Approximation is a map of the circular dichroism (in bright-field) or Circular Intensity Differential Scattering (in dark-field) exhibited by a chiral region inside an object. However, in optically thick (dense) samples, not only these effects, but also the product of linear and circular effects, will contribute to the M_{14} and M_{44} images. The use of imperfect circular polarizations will add additional terms to those already contributing to the true or pure images. These additional terms can be eliminated from the M_{i4} ($i = 1, 4$) images by averaging these entries over an angle of $\pi/2$ about the optical axis.

C. Other Symmetry Considerations in Bright-field Imaging

Any matrix can be expressed as the sum of symmetric and antisymmetric parts. A decomposition of this type for the **Q**-tensor in the expressions in Table I, leads to a number of relationships between the Mueller images. In the bright-field, the tensor $\mathbf{Q} \equiv \mathbf{G}$ (see Table I) and can be written as

$$\mathbf{G} = \mathbf{S} + \mathbf{A} = \begin{bmatrix} S_{xx} & S_{xy} \\ S_{yx} & S_{yy} \end{bmatrix} + \begin{bmatrix} 0 & A_{xy} \\ A_{yx} & 0 \end{bmatrix},$$

where S and A stand for symmetric and antisymmetric, respectively. Here we take $+z$-axis as the direction of propagation of the transmitted light, so that G_{iz} and G_{zj} ($i, j = x, y, z$) need not be considered. It should be noted that $S_{xy} = S_{yx}$ and $A_{xy} = -A_{xy}$, since $\mathbf{S} \equiv (\mathbf{G} + \mathbf{G}^{\mathrm{T}})/2$ and $\mathbf{A} \equiv (\mathbf{G} - \mathbf{G}^{\mathrm{T}})/2$. Rewriting the equations of Table I in terms of the elements of **S** and **A** leads to relationships between the Mueller elements depending on the type of medium considered. We carried out these computations for four different media: (*a*) linearly and circularly isotropic; (*b*) circularly anisotropic; (*c*) linearly anisotropic; and (*d*) linearly and circularly anisotropic.

For an isotropic medium (case *a*), **G** can be written as a constant times a unit tensor. As discussed in paper I, the antisymmetric part of the tensor **G** comes from the chiral nature of a medium. Therefore, the Mueller elements of a medium with only linear anisotropy (case *c*) are expressed in terms of the four components of **S** and their complex conjugates. For a chiral medium (case *b*), both **S** and **A** are needed. However, in this case **S** is a diagonal matrix with $S_{xx} = S_{yy}$ and $S_{xy} = S_{yx} = 0$. In the case of a linearly and circularly anisotropic medium, no such simplifications exist, and the Mueller elements are expressed in terms of the six tensor components and their complex conjugates. Applying these considerations to the Mueller elements in Table I we have obtained the relationships shown below in matrix form for the different media. Here, the Mueller elements are normalized in the same way as in Table I of paper I and we use Perrin's notation (30) to label the elements of the Mueller matrix. Using this notation, we present only the relationships among the 16 Mueller elements for four different media and do not show the explicit equations obtained in terms of the components of **S** and **A**. In the next section (section IV), we show how each element is related to specific physical effects.

Linearly and circularly isotropic:

$$\begin{pmatrix} 1 & 0 & 0 & 0 \\ 0 & 1 & 0 & 0 \\ 0 & 0 & 1 & 0 \\ 0 & 0 & 0 & 1 \end{pmatrix}.$$

Circularly anisotropic:

$$\begin{pmatrix} a_1 & 0 & 0 & b_5 \\ 0 & a_2 & b_4 & 0 \\ 0 & -b_4 & a_2 & 0 \\ b_5 & 0 & 0 & a_1 \end{pmatrix}.$$

Linearly anisotropic:

$$\begin{pmatrix} a_1 & b_1 & b_3 & 0 \\ b_1 & a_2 & b_4 & b_6 \\ b_3 & b_4 & a_3 & b_2 \\ 0 & -b_6 & -b_2 & a_4 \end{pmatrix}.$$

Linearly and circularly anisotropic: In this case, all 16 images, corresponding to the elements of the Mueller matrix for an oriented object, are different.

IV. EXPRESSIONS OF THE BRIGHT-FIELD MUELLER ELEMENTS IN TERMS OF PHENOMENOLOGICAL COEFFICIENTS

It is possible to describe the response of a medium to light by means of phenomenological optical coefficients expressing the absorptive and diffractive properties of the medium. These coefficients are: linear dichroism, linear birefringence, circular dichroism, circular birefringence, mean refraction, and mean extinction.

The form of the Mueller elements in terms of these optical coefficients is particularly simple and allows us to establish relationships among the different entries. Furthermore, they explicitly relate the magnitude and sign of the matrix elements to the macroscopic properties of total absorption, refraction, dichroism, and birefringence.

In this section, the media discussed in section III (part C) are again considered. All but the last of these cases can easily be treated by this macroscopic description. For simplicity we will present the results for the first three cases and will briefly discuss the last case following the method reviewed by Schellman and Jensen (31). In the third case (linearly anisotropic medium), it is assumed that the light propagates along the optical axis of the medium. This assumption greatly simplifies the results obtained. Strictly speaking the results of this section are valid only for samples that are homogeneous along the direction of propagation of the light or for very thin optical paths. Again generalization to optically thick or inhomogeneous media requires more elaborate treatments (31).

To describe the linear anisotropy of a medium, we must define the extinction coefficients $\epsilon_{//}$ and $\epsilon_{\perp}$ and the real refractive indices $n_{//}$ and $n_{\perp}$. These coefficients are along parallel and perpendicular directions relative to an arbitrary fixed laboratory frame. The extinction coefficients $\epsilon_{//,\perp}$ measured in a bright-field experiment have two contributions:

$$\epsilon_{//,\perp} = a_{//,\perp} + s^{\theta}_{//,\perp},$$

where a is the usual absorption coefficient of the medium and s^{θ} is the scattering coefficient. The latter describes the energy removed from the main beam due to scattering away from the forward direction and not captured by the lens' aperture. This contribution is labeled with the superscript θ since it depends on the acceptance angle (θ) of the lens. The scattering coefficient s^{θ} can be related to the molecular scattering cross-section $\sigma(\theta, \phi)$ by (32)

$$s^{\theta}_{//,\perp} = \frac{N_0}{2{,}303} \int_{\theta/2}^{\pi} \int_{0}^{2\pi} \sigma(\theta, \phi) \sin\theta \, d\phi \, d\theta.$$

In practice, the relative importance of this scattering contribution to bright-field images can be made smaller or larger by choosing the appropriate numerical aperture for the objective lens, i.e., by varying θ.

Similarly, the chiral nature (circular anisotropy) of the medium is described by the extinction coefficients (ϵ_R and ϵ_L) and the refractive indices (n_R and n_L) for right- and left-circularly polarized light.

A. Linearly and Circularly Isotropic Medium

This case is almost trivial since it shows no preferential response to any polarization of the incident light. In this case all off-diagonal elements of the Mueller matrix are zero. Only two phenomenological optical constants are required in this case: the total extinction and the mean refraction.

B. Circularly Anisotropic Medium

(*a*) The elements of the twofold symmetric class all vanish as shown in section III, i.e.,

$$\{M_{12}, M_{13}, M_{21}, M_{31}, M_{42}, M_{43}, M_{24}, M_{34}\} = 0.$$

This result is to be expected since an isotropic medium is invariant to rotations about the direction of incidence of the light and the elements in this class change sign under a $\pi/2$ rotation.

(*b*) The following expressions hold for the rest of the normalized Mueller elements:

$$\begin{aligned} M_{11} &= M_{44} = 1 \\ M_{14} &= M_{41} = \tanh CD \\ M_{22} &= M_{33} = \cos 2CB \operatorname{sech} CD \\ M_{23} &= -M_{32} = -\sin 2CB \operatorname{sech} CD, \end{aligned} \tag{21}$$

with $CD \equiv \ln 10\,(\epsilon_L - \epsilon_R)\, cd/2$, where c is the concentration of the chiral molecules and d is the thickness of the sample. In this case the transmitted light is elliptically polarized due to the optical activity of the chiral medium. If $\epsilon_L > \epsilon_R$, the transmitted light is right-elliptically polarized (i.e., the polarization vector rotates in the clockwise sense as viewed by an observer facing the light source). If $\epsilon_R > \epsilon_L$, then the transmitted light is left-elliptically polarized. $CB \equiv 2\pi(n_R - n_L)d/\lambda_0$, where λ_0 is the wavelength of light in vacuum. Thus, CB is the inclination angle (in radians) of the ellipse with respect to the horizontal axis in the case of M_{22} and M_{32}, and with respect to the -45^0 axis in the case of M_{23} and M_{33}. For $CB > 0$, the inclination angle is positive, i.e., it represents a counter-clockwise rotation of the incident linear polarization. Notice that M_{23} and M_{32} are proportional to sin $2CB$, and thus they are sensitive to the optical rotatory power of the medium. Also notice that $M_{14} = M_{41} = \tanh CD$, which means that these two elements contain the contribution from the circular dichroism of the medium. According to the definitions of the extinction coefficients given above, the circular dichroism (CD) includes contributions from the preferential

absorption and scattering of opposite circular polarizations away from the main beam. $M_{11} = M_{44} = 1$ because the Mueller elements are normalized by M_{11}. If unnormalized, M_{11} and M_{44} are related to the mean extinction and mean refraction of the medium.

C. Linearly Anisotropic Medium

The following relationships are obtained in the first Born-Approximation:

$$
\begin{aligned}
M_{11} &= 1 \\
M_{12} &= M_{21} = \cos 2\alpha \tanh (LD)_{II,\perp} \\
M_{13} &= M_{31} = -\sin 2\alpha \tanh (LD)_{II,\perp} \\
M_{14} &= M_{41} = 0 \\
M_{22} &= \cos^2 2\alpha + \sin^2 2\alpha \cos (LB)_{II,\perp} \operatorname{sech} (LD)_{II,\perp} \\
M_{23} &= M_{32} = (1/2) \sin 4\alpha \\
&\quad \cdot [\cos (LB)_{II,\perp} \operatorname{sech} (LD)_{II,\perp} - 1] \\
M_{24} &= -M_{42} = \sin 2\alpha \sin (LB)_{II,\perp} \operatorname{sech} (LD)_{II,\perp} \\
M_{33} &= \sin^2 2\alpha + \cos^2 2\alpha \cos (LB)_{II,\perp} \operatorname{sech} (LD)_{II,\perp} \\
M_{34} &= -M_{43} = \cos 2\alpha \sin (LB)_{II,\perp} \operatorname{sech} (LD)_{II,\perp} \\
M_{44} &= \cos (LB)_{II,\perp} \operatorname{sech} (LD)_{II,\perp}
\end{aligned} \tag{22}
$$

where α is the angle between the parallel (ll) axis of the medium and the vertical (V) axis of a laboratory frame (see Fig. 8), and $(LD)_{II,\perp} \equiv \ln 10\,(\epsilon_{II} - \epsilon_\perp)\,cd/2$. $(LB)_{II,\perp} \equiv 2\pi(n_\perp - n_{II})d/\lambda_0$ is the phase difference induced by the medium between the perpendicular and parallel components of the light. Again $M_{11} = 1$ because it is divided by itself. Notice that M_{12}, M_{13}, M_{21}, and M_{31} are proportional to $\tanh (LD)_{II,\perp}$, which means that these elements are sensitive to the linear dichroism of the sample. Also, it should be noticed that M_{24}, M_{42}, M_{34}, and M_{43} are proportional to $\sin(LB)_{II,\perp}$, which implies that these elements are sensitive to the linear birefringence of the medium.

D. Linearly and Circularly Anisotropic Medium

In this case, the derivation of the Mueller elements is not as simple as in the previous cases. Therefore, we will briefly discuss the method recently reviewed by Schellman and Jensen (31). These authors define six physical effects: linear dichroism (LD) and linear birefringence (LB) along the horizontal and vertical direction with respect to an arbitrary laboratory frame, linear dichroism (LD') and linear birefringence (LB') along the +45°- and −45°-directions with respect to the horizontal direction, and circular dichroism (CD) and circular birefringence (CB). The additional linear effects (LD' and LB') are necessary because they define the optical coefficients with respect to a fixed laboratory coordinate system, whereas in the previous section the optical coefficients (ϵ_{II} and $\epsilon_\perp$) were

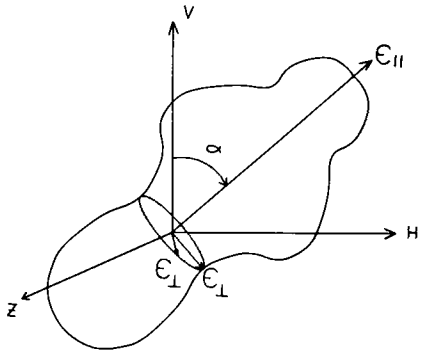

FIGURE 8 An anisotropic object whose parallel (‖) axis is tilted by an angle α with respect to the vertical (V) incident polarization of light.

defined with respect to the molecular frame. Schellman and Jensen also define a general complex retardation for each dichroism-birefringence pair and a total absorption-mean refraction (χ) such that

$$
\begin{aligned}
\chi &= \chi' - iE/2 \\
L &= LB - iLD \\
L' &= LB' - iLD' \\
C &= CB - iCD,
\end{aligned} \tag{23}
$$

where χ' is the change in phase relative to the case where there is no sample and $E = 2.303\,\epsilon cd$ describes the mean extinction of the sample. Thus, the Jones matrix of an isotropic medium is $e^{-i\chi}\begin{pmatrix}1&0\\0&1\end{pmatrix}$. The definitions of CD and CB are as before, and those of LB, LD, LB', and LD' are

$$
\begin{aligned}
LB &= 2\pi(n_x - n_y)d/\lambda_0 \\
LD &= \ln 10(\epsilon_x - \epsilon_y)cd/2 \\
LB' &= 2\pi(n_{+45°} - n_{-45°})d/\lambda_0 \\
LD' &= \ln 10(\epsilon_{+45°} - \epsilon_{-45°})cd/2.
\end{aligned}
$$

Again here it should be noted that LD and LD' contain contributions from both preferential absorption and scattering of linear polarizations. One can define four 2 × 2 Jones matrices (31) corresponding to each of the above general retardations (Eq. 23). In the last three general retardations, the matrices corresponding to dichroism and birefringence on each line commute with one another. However, the matrices corresponding to different general retardations (on different lines) do not commute. This means that, for example, LD and LB measurements do not interfere with each other, i.e., the presence of one does not affect the measurement of the other. On the other hand, LB' or CD affect LD measurements, leading to experimental artifacts. Thus, for optically thick and inhomogeneous samples, the optical effects cannot in general be separated, and they combine their contributions to the measurement of the individual effects. However, for an infinitesimally thin layer of a sample, the three matrices corresponding to the last three general retardations commute with one another to first order. In this case, an infinitesimally thin

sample, with all four optical properties (χ, L, L', C) can be represented as the product of the four infinitesimal Jones matrices. Thus, in the limit of infinitesimally thin samples, the Jones matrix is (to a first-order approximation)

$$\begin{pmatrix} 1 - i\chi - \frac{iL}{2} & -\frac{iL'}{2} + \frac{C}{2} \\ -\frac{iL'}{2} - \frac{C}{2} & 1 - i\chi + \frac{iL}{2} \end{pmatrix}.$$

Taking the limit such that the number of layers goes to infinity and transforming it into a 4 × 4 Mueller matrix, we can obtain the general Mueller matrix for a sample containing the mixing of all eight optical effects. The 16 elements of this general Mueller matrix for a sample with a finite thickness display then the mixing of the physical effects (31). However, when a sample is infinitesimally thin, each Mueller image can (to a first-order approximation) be related to only one pure optical effect according to

$$\begin{pmatrix} 1-E & -LD & -LD' & CD \\ -LD & 1-E & CB & LB' \\ -LD' & -CB & 1-E & -LB \\ CD & -LB' & LB & 1-E \end{pmatrix}. \tag{24}$$

This matrix can be derived by transforming the 2 × 2 Jones matrix for an infinitesimal layer of a sample with all four optical properties in Eqs. 23, into a 4 × 4 Mueller matrix and keeping only the first order terms.

The above infinitesimal Mueller matrix valid in the bright-field geometry is particularly useful for differential polarization microscopy because, for optically thin samples, it relates each Mueller image to a single optical property.

V. OPTICAL RESOLUTION IN DIFFERENTIAL POLARIZATION IMAGING

A. Spatial Resolution

Imaging can be thought of as a mapping process in which to every domain in the object space, S_0, is associated a domain in the image space, S_i. Such mapping can be expressed in its most general form as

$$I: S_0 \longrightarrow S_i.$$

The object and image spaces are defined as collections of distinguishable domains. In practice the imaging process differs from mathematical mapping in that not every geometric element of the object space (point) is associated with a point in the image space. Instead several adjacent elements of the object space are associated with the same elements of the image space. The smallest domain into which the object can be subdivided, so that each domain in the object space corresponds to a distinct domain in the image space, is called the spatial resolution of the imaging system. The size of these domains is controlled and defined by the wavelength of light and the imaging mechanism.

In differential polarization imaging, the mechanism that allows us to distinguish adjacent domains in the object as distinct domains in the image is the ability of these domains to interact differently with light of orthogonal polarizations. The question of interest is then, what is the optical resolution of a differential polarization imaging instrument? In this section, we shall answer this question and establish the limitations on the resolution imposed by the nature of the differential imaging process.

In what follows we will concentrate on the case of linearly anisotropic domains, because their treatment is somewhat simpler. Nonetheless our conclusion can be easily extended to domains possessing both linear and circular anisotropy.

Let two distinct adjacent domains in an object be arranged so that their geometric centers of mass are separated by a distance Y. The origin of the coordinate system for the object is centered on the first group and the second group is on the positive x-axis. For simplicity, we will choose these two domains such that their polarizable axes are along orthogonal directions (the first axis is horizontal and the other is vertical). This choice is made to maximize their differential interaction with the incident orthogonal polarizations of the light. In practice this analysis requires only that the two domains have opposite anisotropies. This restriction amounts to optimizing the estimates on resolution attainable in differential polarization imaging, but the conclusions and trends to be established here will be generally valid for less restricted cases.

Let horizontally polarized light be incident on the sample. Then the intensity distribution in the image plane in dark-field imaging can be written (see paper I):

$$I_H = A\hat{\epsilon}_H \cdot \left[\sum_i e^{+i\Delta k' \cdot r_i} \frac{J_1\left(\frac{ka\rho_i}{r}\right)}{\frac{ka\rho_i}{r}} \alpha_i^\dagger \right] \cdot \mathbf{L} \cdot \left[\sum_j e^{-i\Delta k' \cdot r_j} \frac{J_1\left(\frac{ka\rho_j}{r}\right)}{\frac{ka\rho_j}{r}} \alpha_j \right] \cdot \hat{\epsilon}_H.$$

For vertically polarized light,

$$I_V = A\hat{\epsilon}_V \cdot \left[\sum_i e^{+i\Delta k' \cdot r_i} \frac{J_1\left(\frac{ka\rho_i}{r}\right)}{\frac{ka\rho_i}{r}} \alpha_i^\dagger \right] \cdot \mathbf{L} \cdot \left[\sum_j e^{-i\Delta k' \cdot r_j} \frac{J_1\left(\frac{ka\rho_j}{r}\right)}{\frac{ka\rho_j}{r}} \alpha_j \right] \cdot \hat{\epsilon}_V.$$

Notice that

$$I_H \propto \left[\frac{J_1(X)}{X}\right]^2 \tag{25}$$

and

$$I_V \propto \left[\frac{J_1(X-b)}{X-b}\right]^2 \tag{26}$$

where $X = ka\rho_1/r$ and $X - b = ka\rho_2/r$. b is related to the intergroup distance Y, by $Y = \lambda_0 b/(2\pi n \sin\theta)$. (Refer to paper I for the notation.) The maxima of I_H and I_V appear at the points $X = 0$ and $X = b$, respectively. In general, the values of I_H and I_V need not be equal. Taking them such that $I_V = h\ I_H$, where h is a positive constant, the unnormalized M_{12} element for this object can be written as

$$M_{12} = \frac{I_H - I_V}{2I_0} = \frac{t\left\{\left[\frac{J_1(X)}{X}\right]^2 - h\left[\frac{J_1(X-b)}{X-b}\right]^2\right\}}{2I_0}, \tag{27}$$

where t is the proportionality constant, which depends on the magnitude of α and on the imaging geometry. The numerator of this expression determines the spatial resolution of the imaging system. Fig. 9 shows a plot of this term (*solid line*) for a value of b smaller than 3.833 where the first minima of $[J_1(X)/X]^2$ appears. Also appearing in this figure are the individual terms that make up this difference as given by Eqs. 25 and 26. The calculation corresponds to the choice of $h = 1$ and $t = 1$. Notice that the intensity distribution of M_{12} (*solid line* in Fig. 9) shows a maximum and a minimum whose positions do not coincide with the center of mass of the two distinct domains present in the object. The position of these extrema can be obtained from the condition that the first derivative of the numerator in Eq. 27 vanishes, i.e.,

$$\frac{d\,M_{12}}{d\,X} = \frac{t}{I_0}\left\{\left[\frac{J_1(X)}{X}\right]\left[\frac{J_2(X)}{X}\right] - h\left[\frac{J_1(X-b)}{(X-b)}\right]\left[\frac{J_2(X-b)}{(X-b)}\right]\right\} = 0. \tag{28}$$

It is seen that since a differential polarization image is always a difference of two or more images, the presence of two adjacent domains in the object possessing opposite anisotropies will give rise to the bimodal behavior depicted in Fig. 9. However, as the centers of mass of the domains are brought closer together the intesity of M_{12} and the distance between the extrema both decrease. The decrease of the intensity is shown in Fig. 10 (*solid line*) as a function of the intergroup distance b. The intensity of the extrema can be divided into three different regions. In the first region, for distances between the centers of mass of the domains larger than the Rayleigh criterion, i.e., $X \geq 3.833$ radians, the magnitudes of the extrema are invariant to the

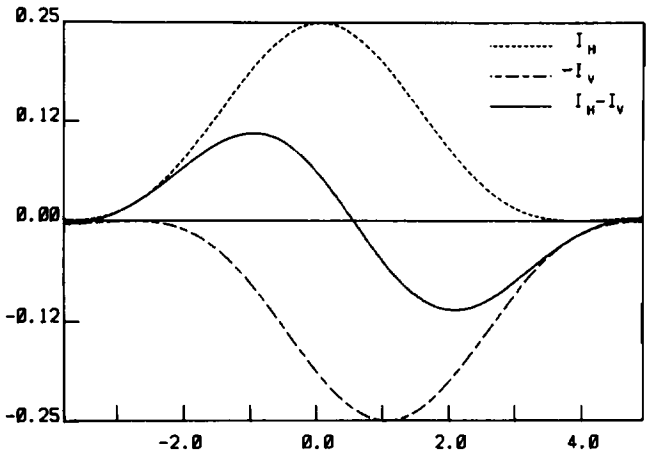

FIGURE 9 A plot of $[J_1(X)/X]^2$ (----), $-[J_1(X-b)/X-b]^2$ (------), and the sum of the previous two terms (——). In this figure, $I_0 = t = h = 1$ and $b = 0.5$.

distance between the domains, as expected from the absence of interference effects. (This region is not shown in Fig. 10.) As the distance between the domains becomes smaller than the Rayleigh limit, the magnitudes of the extrema decrease at a slower rate. For distances much smaller than the wavelength of light, the decrease becomes nearly linear. The dashed line in Fig. 10 shows the behavior of the distance between the extrema, predicted using Eq. 28, as b decreases. Again here three different regions should be distinguished. For distances larger than the Rayleigh criterion, the distance between the extrema decreases linearly as b gets smaller. (This region is not shown in Fig. 10.) For distances smaller than the Rayleigh limit, the rate of approach of the extrema decreases at a slower rate, and finally for distances much closer than the wavelength of light the distance between the extrema asymptotically attains a limit that can be calculated from the solution of Eq. 28.

Thus, in differential polarization imaging when adjacent

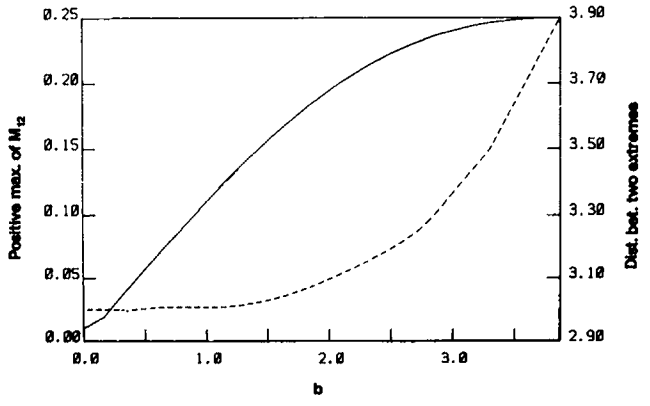

FIGURE 10 The positive maximum value of M_{12} vs. b (——) and the distance between two extrema (positive and the negative extrema) of M_{12} vs. b(----). The scale for the solid line is on the left-hand side and that of dashed line is on the right-hand side.

domains in the object possess opposite anisotropies, the Rayleigh criterion of resolution (as the minimum distance between adjacent domains that can be resolved as distinct in the image) must be replaced by a magnitude criterion. This new criterion establishes that the minimum distance at which two domains can be resolved depends on the limits of sensitivity of the detection. Clearly this bimodal behavior is not present if the adjacent domains possess anisotropies of the same sign. In this case the usual Rayleigh criterion must be used. The above magnitude criterion might allow an improved resolution over the diffraction limitations imposed in regular microscopy if appropriate ultrasensitive detection methods are used. This extended resolution exists only on transitions between regions of opposite anisotropy in the object. It should be pointed out that the above analysis is valid independent of the optical effects responsible for the anisotropy. Thus the conclusions are also valid for any of the six main optical effects already described (*LB*, *LD*, *LB'*, *LD'*, *CB*, *CD*).

To demonstrate what has been said above, we have generated the Mueller images of an object which consists of two uniaxial polarizable groups situated on the x-axis. The polarizable group on the negative x-axis is vertical, and the one on the positive x-axis is horizontal.

The polarizabilities of the groups are chosen to be complex so that both absorption and scattering take place. Fig. 11 shows the M_{11} and M_{12} bright-field images of these two points, separated by a distance of 4.29 λ_0 (*a* and *b*) and 0.57 λ_0 (*c* and *d*), respectively. In Fig. 11 *a* (M_{11}), we see that the two points are well resolved since they are separated by a distance greater than the resolution length (2.515 λ_0). In Fig. 11 *b* (M_{12}), there is one positive lobe (*solid line*) and one negative lobe (*dashed line*). Since the vertically polarizable group absorbs vertically polarized light and does not absorb horizontally polarized light, the differential intensity surrounding this dipole in the M_{12} image should be positive. Likewise, the horizontally polarizable group absorbs horizontally polarized light and does not absorb vertically polarized light, thus the region surrounding this dipole in the M_{12} image should be negative. These two points are also well resolved in the differential image. In Fig. 11 *c*, these groups are now too close together to be resolved by the regular unpolarized image. However, the two dipoles are still well resolved in the M_{12} image (Fig. 11 *d*) because their different orientations manifest themselves as the different intensities and signs in the M_{12} image.

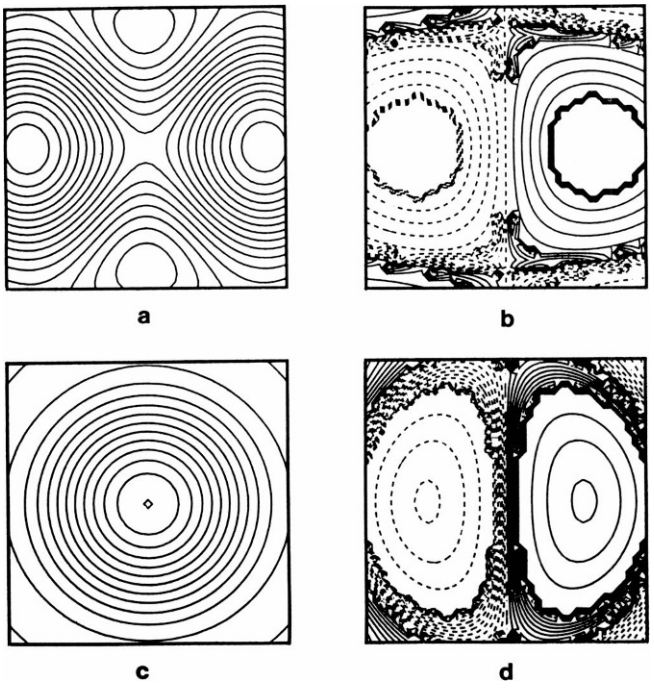

FIGURE 11 Bright-field images of two dipoles separated by a distance greater (*a* and *b*) and shorter (*c* and *d*) than the resolution length of the imaging system. (*a*) M_{11} image. (*b*) M_{12} image. (*c*) M_{11} image. (*d*) M_{12} image.

B. Depth of Field

The theory presented in the previous sections and in the preceding paper are only formally valid for two-dimensional objects, i.e., objects that extend in the x-and y-directions but are infinitely thin along the z-direction. This approximation is introduced by the use of the lens formula in Gaussian form (see Eq. 14 in paper I):

$$\frac{1}{r_0} + \frac{1}{d} - \frac{1}{f} = 0.$$

This formula relates the distance (r_0) between a flat two-dimensional object and the imaging lens (with focal length f), to the distance (d) between the lens and the image plane at which a sharp image of the object is obtained. This approximation greatly simplifies the diffraction integral in Eq. 14 of paper I. It is a result of geometrical optics and does not take into account the diffraction limitations of the imaging process.

In practice the object is not two-dimensional, and for any real lens, there is a finite range of distances along the optical axis within which all parts of the object contained in this thickness are sharply focused in the image plane. This thickness is known as the depth of field of the lens.

Several criteria have been used in the literature to describe the depth of field (33–35). Here, we will use the concept of setting accuracy introduced by Fraçon (36):

$$S = \frac{\lambda_0}{4n \sin^2\left(\frac{\theta}{2}\right)},$$

where n is the refractive index of the immersion medium, λ_0 is the wavelength of the light in vacuum, and θ is the half-cone angle subtended by the objective lens. Since the numerical aperture of the lens is

$$NA = n \sin \theta.$$

It is seen that in general the depth of field of the lens decreases with its numerical aperture.

C. Optical Sectioning

Is the concept of depth of field valid in differential polarization imaging? If so, is optical sectioning of the sample possible in differential polarization imaging?

The answer to the first question is affirmative since the basis of image formation is not altered in differential polarization imaging as was seen in paper I. To answer the second question we must consider two opposite cases: (*a*) when the sample is optically dense and thick, and (*b*) when the sample is optically thin and the light does not experience multiple interactions within the sample.

In the first case, the polarization of the light is modified as the light travels through the medium. In this way, successive layers in the sample experience different polarizations that are not under the direct control of the experimenter. The light preserves a memory so-to-speak of the preceding layers and mixes the effect of these previous interactions with the effect of the successive layers. In this case the problem of extracting structural information from each layer can be very complicated, and the differential slicing methods developed in the theory of Mueller calculus (31) must be used to de-convolute the information of a given layer immersed or sandwiched between the other layers. This program is currently under way in our laboratory, so here we will concentrate only on the second case (when the sample is optically thin).

In the case of optically thin samples, we can readily modify the theory developed in paper I. The expression for the diffraction integral (Eq. 14 in paper I) is

$$\int_{\text{aperture}} \exp ik\left[\frac{(r')^2}{2}\left(\frac{1}{r_0}+\frac{1}{r}-\frac{1}{f}\right)-\left(\frac{\mathbf{r}_i}{r_0}+\hat{\mathbf{r}}\right)\cdot\mathbf{r}'\right]da'.$$

If the Gaussian lens formula is not used, this equation cannot in general be integrated analytically because the integrand no longer has a simple gaussian form. Nonetheless, the integration can be performed numerically.

To understand the concept of optical slicing and depth of field in differential polarization imaging, we have generated the bright-field M_{12} images of a three-dimensional object. The geometry of the model is shown in Fig. 12 *a*, and consists of two thin planes separated by a distance D along the optical axis. The distance D between the planes must be larger than the setting accuracy of the lens in order to resolve the two planes. For apertures that are not too large, the setting accuracy can be approximated by

$$S=\frac{n\lambda_0}{(NA)^2}.$$

Taking $n = 1$ and choosing a numerical aperture of 0.5 means that the minimum distance between the two object planes must be at least four times the wavelength of the light for the lens to resolve them along the optical axis.

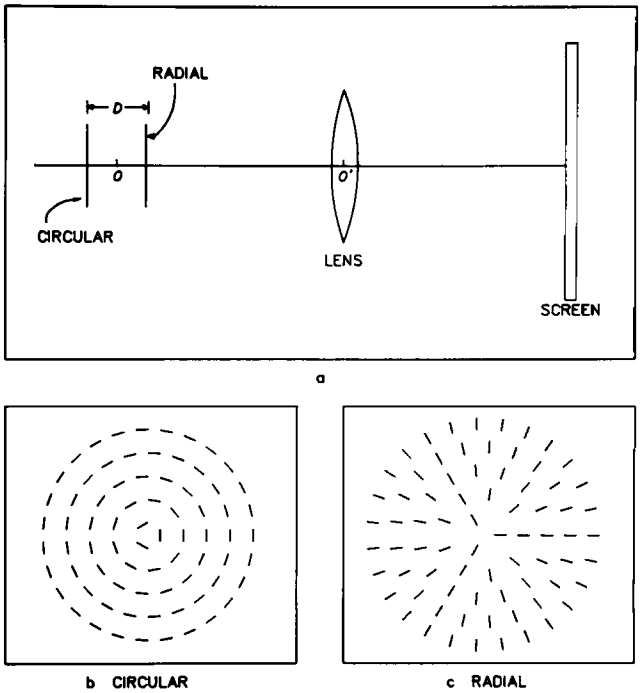

FIGURE 12 Geometry of the model for the differential images shown in Fig. 13. *O* is the point on the optical axis which is in focus. (*a*) The position of radial and circular planes. (*b*) The position and orientation of the uniaxial polarizable groups in the circular plane. (*c*) The position and orientation of the uniaxial polarizable groups in the radial plane. In both planes, the number of groups and their positions are identical. There are 75 groups in each plane.

The plane closest to the lens contains a radial distribution of transition dipole moments as shown in Fig. 12 *c*, and the plane furthest from the lens contains transition dipole moments oriented circularly as shown in Fig. 12 *b*. The distance between the individual groups in each plane is smaller than the wavelength of light. It is possible to focus on either of the two planes by moving both of them together along the optical axis. The M_{12} images of this object are shown in Fig. 13 with $D = 6.5\,\lambda_0$ and $NA = 0.37$. Fig. 13 *c* shows the image obtained when the circular plane is in focus, and Fig. 13 *d* is obtained when the radial plane is in focus. For comparison purposes, the M_{12} image of a single circular layer in focus is shown in Fig. 13 *a* and that of a single radial layer in focus is shown in Fig. 13 *b*. Thus, it can be seen that the images obtained by focusing on the radial or circular plane of the layered object have the same spatial distribution of sign as the images of a single radial or circular layer. However, because at every point in the object the dipoles of the radial and circular layers are orthogonal, if D is less than the setting accuracy of the imaging system, the contributions of the two planes to the M_{12} images cancel each other out and the individual contributions cannot be separated in the M_{12} image.

The above result shows that it is possible to do optical sectioning in differential polarization imaging provided that the sample is not too optically dense. In this case the

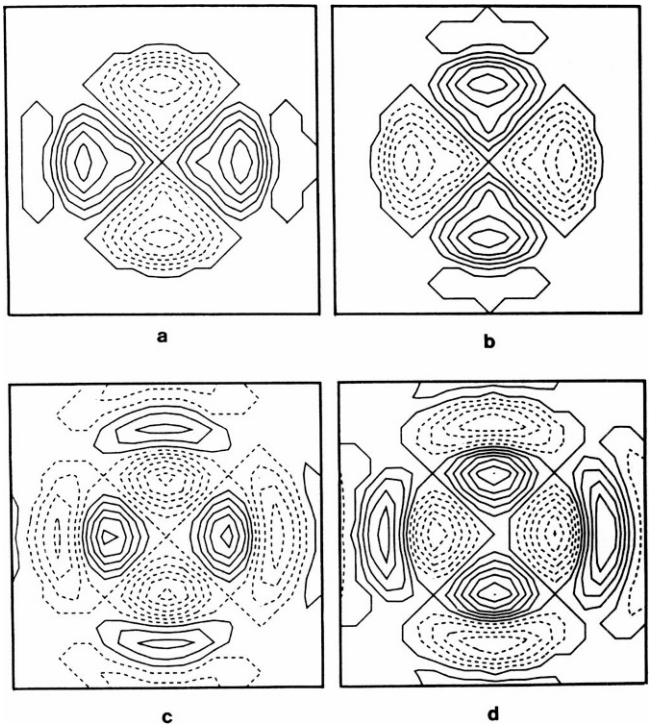

FIGURE 13 M_{12} images of radial and circular plane models. (*a*) M_{12} image of only the circular plane (as drawn in Fig. 12 *b*) placed at the point *O* (see Fig. 12 *a*). (*b*) M_{12} image of only the radial plane (as drawn in Fig. 12 *c*) placed at the point *O*. (*c*) M_{12} image of both circular and radial planes. Two planes are simultaneously shifted toward the lens compared with Fig. 12 *a* so as to have the circular plane in focus. $D = 6.5\,\lambda_0$. (*d*) M_{12} images of both circular and radial planes. Two planes are simultaneously shifted to left compared with Fig. 12 *a* so as to have the radial plane in focus. $D = 6.5\,\lambda_0$. For these computations, r_0, a, and n are chosen so that the resolution length of the imaging system is $1.64\,\lambda_0$.

optical depth resolution is controlled by the setting accuracy on the lens.

VI. CONCLUSIONS

The main properties of the Mueller images discussed in this paper are summarized as follows: (*a*) The 16 Mueller images were divided into three classes according to their symmetry behavior upon a rotation of the optical components about the optical axis of the imaging system. The elements in the first class, which are invariant to rotation, are M_{11}, M_{14}, M_{41}, and M_{44}. The elements in class II (M_{12}, M_{13}, M_{21}, M_{31}, M_{42}, M_{43}, M_{24}, and M_{34}) change sign upon a rotation of $\pi/2$ radians and reproduce themselves after a rotation of π radians. The rest of the elements, M_{22}, M_{23}, M_{32}, and M_{33}, belong to the thrid class and these elements reproduce themselves after $\pi/2$ radians. However, they do not change sign upon a rotation of $\pi/4$ radians.

(*b*) Using the fact that the M_{14} and M_{44} images are invariant upon rotation, it is possible to eliminate the artifacts in these images due to imperfections in the incident circular polarizations.

(*c*) Phenomenological equations for the bright-field Mueller elements were derived for four different media: (*a*) linearly and circularly isotropic, (*b*) circularly anisotropic, (*c*) linearly anisotropic, and (*d*) linearly and circularly anisotropic. The relationships among the 16 bright-field Mueller elements, obtained by comparing the phenomenological equations, are the same as those obtained by decomposing the G-tensor into symmetric (S) and antisymmetric (A) parts and expressing the 16 Mueller elements in terms of the components of the S- and A-tensors.

It was shown that, when a sample has a chiral structure, M_{14} and M_{41} are sensitive to the circular dichroism, and M_{23} and M_{32} are sensitive to the optical rotatory power. When a sample is linearly anisotropic, M_{12}, M_{13}, M_{21}, and M_{31} are sensitive to linear dichroism, and M_{24}, M_{34}, M_{42}, and M_{43} are sensitive to linear birefringence. For an optically thin sample with mixed anisotropies, the off-diagonal elements of the Mueller matrix are sensitive to the same optical effects as the Mueller matrix elements of a medium with only one kind of anisotropy, and the diagonal elements are identical to M_{11}.

(*d*) If two adjacent domains have different preferences to the incident polarization, the limit of resolution in differential polarization imaging is not restricted by the Rayleigh criterion but instead depends on the detection sensitivity.

(*e*) It was shown that three-dimensional sectioning is possible in differential polarization imaging. This was illustrated by the M_{12} images of an object composed of two different planes separated by $6.5\,\lambda_0$ along the optical axis. When the distance between two planes along the optical axis is larger than the setting accuracy of the imaging system, the M_{12} images of two planes were resolved.

This work was supported in part by a grant from the National Institutes of Health GM-32543, National Science Foundation DMB-8609654 and DMB-8501824, a 1984 Searle's Scholarship, and an Alfred P. Sloan Fellowship. Additional support was obtained from the Center of High Technology and Materials, UNM. C. Bustamante is a 1984 Searle Scholar and a 1985 Alfred P. Sloan Fellow.

Received for publication 14 April 1987 and in final form 7 August 1987.

REFERENCES

1. Mickols, W., I. Tinoco, Jr., J. E. Katz, M. F. Maestre, and C. Bustamante. 1985. Imaging differential polarization microscope with electronic readout. *Rev. Sci. Instrum.* 56:2228–2236.
2. Beach, D. A., K. S. Wells, F. Husher, and C. Bustamante. 1987. Differential polarization microscope using an image dissector camera and phase-lock detection. *Rev. Sci. Instrum.* In press.
3. Mickols, W., M. F. Maestre, I. Tinoco, Jr., and S. H. Embury. 1985. Visualization of oriented hemoglobin S in individual erythrocytes by differential extinction of polarized light. *Proc. Natl. Acad. Sci. USA.* 82:6527–6531.
4. Klug, A., J. T. Finch, and T. J. Richmond. 1985. Crystallographic structure of the octamer histone core of the nucleosome. *Science (Wash. DC).* 229:1109–1113.
5. Klug, A., D. Rhodes, J. Smith, and J. T. Finch. 1980. A low resolution structure for the histone core of the nucleosome. *Nature (Lond.).* 287:509–516.

6. Finch, J. T., R. S. Brown, D. Rhodes, T. Richmond, B. Rushton, L. C. Lutter, and A. Klug. 1981. X-ray diffraction study of a new crystal form of the nucleosome core showing higher resolution. *J. Mol. Biol.* 145:757–769.
7. Bentley, G. A., J. T. Finch, and A. Lewit-Bentley. 1981. Neutron diffraction studies on crystals of mucleosome cores using contrast variation. *J. Mol. Biol.* 145:771–784.
8. Jordano, J., M. A. Nieto, and E. Palacian. 1985. Dissociation of nucleosomal particles by chemical modification. *J. Biol. Chem.* 260:9382–9384.
9. Richmond, T. J., A. Klug, J. T. Finch, and L. C. Lutter. 1981. The organization of DNA in the nucleosome core particle. *Proceedings of the Second SUNYA Conversation in the Discipline Biomolecular Stereodynamics.* Adenine Press, New York. 2:109–123.
10. Wang, J. C. 1982. The path of DNA in the nucleosome. *Cell.* 29:724–726.
11. Klug, A., L. C. Lutter, and D. Rhodes. 1982. Helical periodicity of DNA on and off the nucleosome as probed by nucleases. *Cold Spring Harbor Symp. Quant. Biol.* 47:285–292.
12. Mirzabekov, A. D., S. G. Bavykin, V. L. Karpov, O. V. Preobrazhenskaya, K. K. Ebralidze, V. M. Tuneev, A. F. Melnikova, E. G. Goguadze, A. A. Chenchick, and R. S. Beabealashvili. 1982. Structure of nucleosomes, chromatin, and RNA polymerase-promoter complex as revealed by DNA-protein cross-linking. *Cold Spring Harbor Symp. Quant. Biol.* 47:503–510.
13. Ibel, K., R. Klingholz, W. H. Straetling, J. Bogenberger, and F. Fittler. 1983. Neutron diffraction of chromatin in interphase nuclei and metaphase chromosomes. *Eur. J. Biochem.* 133:315–319.
14. Butler, P. J. G. 1984. A defined structure of the 30nm chromatin fiber which accommodates different nucleosomal repeat lengths. *EMBO (Eur. Mol. Biol. Organ.) J.* 3:2599–2604.
15. Mitra, S., S. Dipankar, and D. M. Crothers. 1984. Orientation of nucleosomes and linker DNA in calf thymus chromatin determined by photochemical dichroism. *Nature (Lond.).* 308:247–250.
16. Karnik, P. S. 1983. Correlation between phosphorylated H1 histone and condensed chromatin in Planococcus citri. *FEBS (Fed. Eur. Biochem. Soc.) Lett.* 163:128–131.
17. Huang, H., and R. D. Cole. 1984. The distribution of H1 histone is nonuniform in chromatin and correlates with different degrees of condensation. *J. Biol. Chem.* 259:14237–14242.
18. Glotov, B. O., L. G. Nikolaev, V. K. Dashkevich, and S. F. Barbashov. 1985. Histone crosslinking patterns indicate dynamic binding of histone H1 in chromatin. *Biochim. Biophys. Acta.* 824:185–193.
19. Weith, A. 1985. The fine structure of euchromatin and centromeric hetero-chromatin in Tenebrio molitro chromosomes. *Chromosoma (Berl.).* 91:287–296.
20. Seki, S., T. Nakamura, and T. Oda. 1984. Supranucleosomal fiber loops of chicken erythrocyte chromatin. *J. Electron Microsc.* 33:178–181.
21. Barbashov, S. F., B. O. Glotov, and L. G. Nikolaev. 1984. Evidence for attachment of interphase chromatin to the nuclear matrix via matrix-bound nucleosomes. *Biochim. Biophys. Acta.* 782:177–186.
22. Becak, M. L., K. Fukuda-Pizzocaro, R. de C. Santos, and O. Brunner. 1985. Circular chromatin complexed in human lymphocytes. High-resolution autoradiography. *Rev. Bras. Genet.* 8:97–106.
23. Earnshaw, W. C., N. Halligan, C. Cooke, and N. Rothfield. 1984. The kinotochore is part of the metaphase chromosome scaffold. *J. Cell Biol.* 98:353–357.
24. Nielson, P. E., Y. Matsuoka, and B. J. F. Norden. 1985. Stepwise unfolding of chromatin by urea. A flow linear dichroism and photoaffinity labeling study. *Eur. J. Biochem.* 147:65–68.
25. Lebkowski, J. S., and U. K. Laemmli. 1982. Evidence for two levels of DNA folding in histone-depleted HeLa interphase nuclei. *J. Mol. Biol.* 156:309–324.
26. Prusov, A. N., V. Yu. Polyakov, O. V. Zatsepina, Yu. S. Chentsov, and D. Fais. 1983. Rosette-like structures from nuclei with condensed (chromomeric) chromatin but not from nuclei with diffuse (nucleomeric or nucleosomic) chromatin. *Cell Biol. Int. Rep.* 7:849–858.
27. Leon, P., and G. Macaya. 1985. Properties of DNA rossettes and their relevance to chromosome structure. *Chromosoma (Berl.).* 88:307–314.
27a. Langmore, J. P., and J. R. Paulson. 1983. Low angle x-ray diffraction studies of chromatin structure in vivo and in isolated nuclei and metaphase chromosomes. *J. Cell Biol.* 96:1120–1131.
28. Landau, L. D., and E. M. Lifshitz, 1969. Mechanics. 2nd ed. Pergamon Press, Oxford, New York.
29. Goldstein, H. 1981. Classical Mechanics. Addison-Wesley Publishing Co. Inc., Reading, MA.
30. Perrin, F. 1942. Polarization of light scattered by isotropic opalescent media. *J. Chem. Phys.* 10:415–427.
31. Schellman, J. A., and H. P. Jensen. 1987. Phase modulation spectroscopy. *Chem. Rev.* In press.
32. Bustamante, C., I. Tinoco, Jr., and M. F. Maestre. 1983. Circular differential scattering can be an important part of the circular dichroism of macromolecules. *Proc. Natl. Acad. Sci. USA.* 80:3568–3572.
33. Inoue, S. 1986. Video Microscopy. Plenum Press, New York. 118.
34. Martin, L. C. 1966. The Theory of Microscope. American Elsevier, New York.
35. Piller, H. 1977. Microscope Photometry. Springer-Verlag, Berlin.
36. Françon, M. 1961. Progress in Microscopy. Row, Peterson, Evanston, IL.